Scientia Pharmaceutica

ÖSTERREICHISCHE PHARMAZEUTISCHE GESELLSCHAFT

MDPI

Article

Orotic Acid–1,2,4-Triazole Hybrids as Potential MMP-2,9 Modulating Wound-Healing Agents: Synthesis, Molecular Docking and Biological Evaluation

Yuriy Karpenko [1,*], Volodymyr Parchenko [1], Lyudmila Kucherenko [2], Tetiana Chetvertak [3], Oleksii Bihdan [4], Iryna Pukhalska [5], Olena Roik [6], Daria Safronova [5], Ihor Meladze [7] and Inna Bushueva [8]

1 Department of Toxicological and Inorganic Chemistry, Zaporizhzhia State Medical and Pharmaceutical University, 69035 Zaporizhzhia, Ukraine; parchenko@ukr.net
2 Department of Pharmaceutical, Organic and Bioorganic Chemistry, Zaporizhzhia State Medical and Pharmaceutical University, 69035 Zaporizhzhia, Ukraine; kucherenko.l.i@mphu.edu.ua
3 Department of Chemistry and Chemical Education, Bogdan Khmelnitsky Melitopol State Pedagogical University, 69061 Zaporizhzhia, Ukraine; tetiana.chetvertak@mspu.edu.ua
4 Department of Clinical Pharmacy, Pharmacotherapy, Pharmacognosy and Pharmaceutical Chemistry, Zaporizhzhia State Medical and Pharmaceutical University, 69035 Zaporizhzhia, Ukraine; bigdan.o.a@mphu.edu.ua
5 Department of Drug Technology, Zaporizhzhia State Medical and Pharmaceutical University, 69035 Zaporizhzhia, Ukraine; pukhalska.i.o@zsmu.edu.ua (I.P.); romaningena0@gmail.com (D.S.)
6 Department of Industrial Pharmacy, Kyiv National University of Technology and Design, 01011 Kyiv, Ukraine; roik.om@knutd.edu.ua
7 Department of Therapeutic, Orthopedic, and Pediatric Dentistry, Zaporizhzhia State Medical and Pharmaceutical University, 69035 Zaporizhzhia, Ukraine; meladze.i.n@mphu.edu.ua
8 Department of Management and Economics of Pharmacy and Pharmaceutical Technology, Zaporizhzhia State Medical and Pharmaceutical University, 69035 Zaporizhzhia, Ukraine; valery999@ukr.net
* Correspondence: karpenko.y.v@gmail.com; Tel.: +380-639734427

Abstract

The matrix metalloproteinases MMP-2 and MMP-9 are involved in extracellular matrix remodeling, inflammatory response, and tissue remodeling, and overactivity of certain metalloproteinases may also contribute to chronic wound healing. The aim of this work was to synthesize novel hybrid derivatives of orotic acid and 1,2,4-triazole and investigate them as potential modulators of MMP-2/MMP-9. The structure of the compounds was confirmed by ^{1}H, ^{13}C NMR spectroscopy, LC–MS, and elemental analysis. Pharmacokinetic properties were calculated using SwissADME, and enzyme interactions were characterized using molecular docking strategies, protein–ligand contact analysis, and 100 ns molecular dynamics. The inhibitory effect was also assessed in vitro by fluorimetry at a concentration of 10 μM. The compounds had an acceptable drug-like profile, without violations of Lipinski's rule and PAINS warnings. The highest affinity for MMP-9 was also found for the three target proteins **17**, **19** and **13**, which showed values of −9.65, −9.47 and −9.17 kcal/mol, respectively, compared to −8.37 kcal/mol for **NNGH**. Dynamic molecular analysis confirmed the stability of the **13**–MMP-9 complex. Compounds 17 and 13 inhibited MMP-9 by 94.2 ± 4.8% and 85.2 ± 3.8%, respectively, with little effect on MMP-2, whereas compound 19 showed balanced inhibition of MMP-2 and MMP-9 by 74.2 ± 4.4% and 79.2 ± 2.8%, respectively. The results identified **13** and **17** as potential compounds with preferential effects on MMP-9, and 19 as a possible dual inhibitor for wound healing activity studies.

Keywords: orotic acid; 1,2,4-triazole; matrix metalloproteinases; MMP-9; MMP-2; molecular docking; molecular dynamics; ADME; wound healing

Academic Editors: Roman B. Lesyk and Monika Wujec

Received: 14 July 2026
Revised: 3 August 2026
Accepted: 3 August 2026
Published: 5 August 2026

1. Introduction

Matrix metalloproteinases (MMPs) are a family of zinc-dependent endopeptidases that are involved in the degradation of extracellular matrix components, tissue remodeling, regulation of intercellular and cell–matrix interactions, angiogenesis, neurogenesis, inflammation, and reparative processes [1–3]. More than 20 representatives of this family have been described in humans, the activity of which is finely regulated by cytokines, hormones, growth factors, tissue inhibitors of metalloproteinases (TIMPs), as well as proteolytic activation of proenzyme forms [1,4]. A special place among MMPs is occupied by gelatinases—MMP-2 and MMP-9, which are able to cleave denatured collagen, type IV collagen, and other structural proteins of the basement membrane, which determines their important role in physiological tissue remodeling and pathological matrix destruction [2,3].

Matrix metalloproteinase-9 (MMP-9, gelatinase B) is one of the most functionally important members of the MMP family. It is secreted predominantly as the inactive proenzyme pro-MMP-9 by various cell types, including endothelial cells, fibroblasts, leukocytes, neutrophils, and macrophages [4,5]. Granulocytic cells are an important source of MMP-9, and neutrophils are considered one of the key cellular reservoirs of this enzyme during inflammation [5,6]. In the central nervous system, MMP-9 expression and activity are associated with neuroplasticity, neuroinflammation, remodeling of synaptic contacts, and disruption of the blood–brain barrier [7,8].

The physiological role of MMP-9 is to control extracellular matrix remodeling, regulate cell migration, tissue repair, and the inflammatory response [3,5]. At the same time, excessive or dysregulated MMP-9 activity is associated with the progression of a number of pathological conditions, including rheumatoid arthritis, cancer, ischemic stroke, neurological and inflammatory processes, and arteriovenous malformations [9–13]. In the context of tissue damage and wound healing, MMP-9 has a dual role: on the one hand, it promotes wound cleansing and matrix remodeling, and on the other hand, its excessive activity can maintain chronic inflammation, disrupt granulation tissue formation, and slow down reparative processes [14,15]. Therefore, controlling the activity of MMP-9, as well as the related gelatinase MMP-2, is considered a promising approach to finding new compounds with potential anti-inflammatory, cytoprotective, and wound healing effects [3,14,15]. Despite the significant interest in inhibiting MMP-2/MMP-9, classical hydroxamate inhibitors such as marimastat, batimastat or GM6001 have limitations associated with insufficient selectivity, excessive chelating activity towards the Zn^{2+} ion and the risk of unwanted inhibition of other metalloproteinases [16,17]. In this regard, a relevant direction is the search for non-hydroxamate heterocyclic inhibitors capable of interacting with the active center of MMP-2/MMP-9 not only through metal coordination, but also through hydrogen bonds, π-interactions, hydrophobic contacts and spatial complementarity to the S1′-pocket of the enzyme [18,19]. The proposed derivatives of orotic acid and 1,2,4-triazole have pharmacophoric similarity with known non-hydroxamate inhibitors of MMP-9/MMP-2 due to the combination of several structurally significant elements: a pyrimidine-2,4-dione core capable of forming donor–acceptor hydrogen interactions; a 1,2,4-triazole-3-thione/S-alkyl fragment as a sulfur-containing heterocyclic pharmacophore; as well as variable alkyl, aryl or heteroaryl substituents that can provide additional hydrophobic and π-contacts in the active site of gelatinases [19–21]. In contrast to classical hydroxamate inhibitors, the studied compounds are not based exclusively on direct Zn^{2+} chelation, but can implement an alternative binding profile, which is promising for increasing selectivity and reducing nonspecific activity [16,17,19].

The rational design of the studied compounds was based on three main factors (Figure 1). First, the inclusion of an orotic/pyrimidine-2,4-dione fragment was considered as a way to enhance hydrogen bonding and mimic the structural motifs of known

pyrimidine-dione/trione MMP inhibitors [20]. Second, the introduction of the 1,2,4-triazole-3-thione/S-alkyl moiety was aimed at creating a sulfur-containing heterocyclic center potentially relevant for interaction with MMP-2/MMP-9 [21]. Third, variation in the substituents in the S-alkyl or amide moiety allows for the regulation of lipophilicity, spatial correspondence to the active site, the intensity of hydrophobic contacts, and potential selectivity towards gelatinases [18,19,22]. Thus, the combination of orotic acid with a 1,2,4-triazole pharmacophore can be considered as a reasonable strategy for the creation of new non-hydroxamate MMP-2/MMP-9 inhibitors with potential wound healing activity.

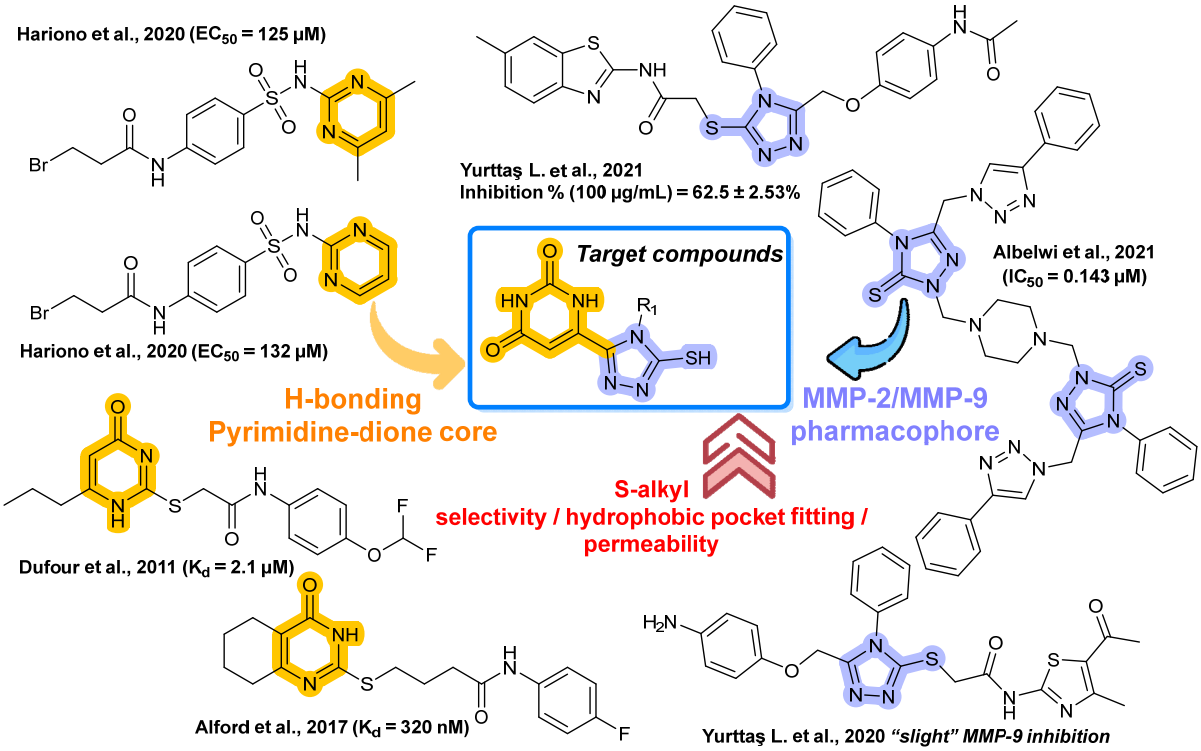

Figure 1. Structural rationale for the design of orotic acid–1,2,4-triazole hybrids as potential MMP-2/MMP-9 inhibitors. Reported MMP-2/MMP-9 inhibitors contain several pharmacophoric motifs relevant to the present study, including pyrimidine-dione/trione scaffolds, 1,2,4-triazole-thione fragments, sulfur-containing linkers, and heteroaryl amide substituents [22–27]. These structural features were integrated into the design of the target orotate–triazole hybrids, combining a pyrimidine-2,4-dione core with a 1,2,4-triazole-3-thione/S-alkyl fragment.

2. Materials and Methods

Chemistry: The ^{1}H, ^{13}C spectra were recorded on a Bruker AC-400, AC-500 spectrometer (100, 125, 500 MHz) in DMSO-d_6, and the internal standard was TMS (Bruker BioSpin GmbH, Rheinstetten, Germany). LC–MS analyses were performed using an Agilent 1260 LC/MSD system (Agilent Technologies, Santa Clara, CA, USA) equipped with a G1315B diode-array detector operating at 215 and 241 nm, a G6140 quadrupole mass detector, and a SofTA 1400 evaporative light-scattering detector (SofTA Corporation, Westminster, CO, USA). Chromatographic separation was carried out on a Zorbax SB-C18 Rapid Resolution HT column (4.6 × 30 mm, 1.8 μm; Agilent Technologies, Santa Clara, CA, USA) using water containing 0.1% formic acid as mobile phase A and acetonitrile containing 0.1% formic acid as mobile phase B. Mass spectra were recorded in positive electrospray ionization mode. Elemental analysis (C, H, N, S) is made on ELEMENTAR vario EL cube (standard-sulfanilamide; Elementar Analysensysteme GmbH, Langenselbold, Germany). The melting points are determined by the capillary method in "Stanford Research Systems Melting

Point Apparatus 100" (Stanford Research Systems, Sunnyvale, CA, USA). Used reagents were purchased from Sigma-Aldrich (Merck KGaA, Darmstadt, Germany).

Orotic acid hydrazide was synthesized according to previously reported procedures [28–30], and its physicochemical constants were consistent with the literature data.

Preparation of 6-(5-mercapto-4-methyl-4H-1,2,4-triazol-3-yl)pyrimidine-2,4(1H,3H)-dione (**2**): Orotic acid hydrazide (10 mmol) was suspended in propan-2-ol (20 mL), and the resulting suspension was heated with stirring. A solution of methyl isothiocyanate (10 mmol) in propan-2-ol (5 mL) was added dropwise. The reaction mixture was heated under reflux for 2 h and then cooled to room temperature. The precipitated 2-(2,6-dioxo-1,2,3,6-tetrahydropyrimidine-4-carbonyl)-*N*-methylhydrazine-1-carbothioamide (**1**) was collected by filtration, dried, and used in the next step without additional purification. A mixture of the obtained carbothioamide (10 mmol), sodium hydroxide (10 mmol), and purified water (20 mL) was heated under reflux for 2 h. After cooling, the reaction mixture was filtered, and the filtrate was acidified with concentrated acetic acid (2 mL). The resulting precipitate was collected by filtration, washed with purified water, dried, and recrystallized from *N*,*N*-dimethylformamide.

2-(2,6-Dioxo-1,2,3,6-tetrahydropyrimidine-4-carbonyl)-*N*-methylhydrazine-1-carbothioamide (**1**). Yield 79%; light-yellow powder; mp 270 °C (DMF). ^{1}H NMR (500 MHz, DMSO-d_6) δ 2.97 (d, J = 4.2 Hz, 3H, NH–CH_3), 6.35 (s, 1H, pyrimidine CH), 7.55 (q, J = 4.2 Hz, 1H, NH–CH_3), 10.23–10.29 (m, 2H, NH–NH), 11.27 (s, 1H, pyrimidine NH), 11.30 (s, 1H, pyrimidine NH). LC-MS (ESI^+), t_R = 0.852 min: *m*/*z* 244.0 $[M + H]^+$. Anal. calcd for $C_7H_9N_5O_3S$: C, 34.57; H, 3.73; N, 28.79; S, 13.18%. Found: C, 34.51; H, 3.91; N, 28.72; S, 13.24%.

6-(5-Mercapto-4-methyl-4H-1,2,4-triazol-3-yl)pyrimidine-2,4(1H,3H)-dione (**2**). *Yield 64%; light-yellow powder; mp 282 °C (DMF).* ^{1}H NMR (500 MHz, DMSO-d_6) δ 3.67 (s, 3H, N–CH_3), 6.11 (s, 1H, pyrimidine CH), 7.01 (s, 1H, SH), 11.16 (s, 1H, NH), 11.70 (s, 1H, NH). LC-MS (ESI^+), t_R = 0.598 min: *m*/*z* 226.0 $[M + H]^+$. Anal. calcd for $C_7H_7N_5O_2S$: C, 37.33; H, 3.13; N, 31.10; S, 14.23%. Found: C, 37.35; H, 3.26; N, 31.11; S, 14.18%.

General procedure for the synthesis of S-alkyl derivatives (**3**–**12**): A mixture of **2** (5 mmol) and sodium hydroxide (5 mmol) in propan-2-ol (10 mL) was prepared. The corresponding alkyl halide (5 mmol) was added, and the reaction mixture was heated under reflux for 2 h. After cooling, the resulting precipitate was collected by filtration, washed with purified water, dried, and recrystallized from methanol.

6-(4-Methyl-5-(methylthio)-4H-1,2,4-triazol-3-yl)pyrimidine-2,4(1H,3H)-dione (**3**). Yield 70%; brown powder; mp 142 °C (MeOH). ^{1}H NMR (500 MHz, DMSO-d_6) δ 2.62 (s, 3H, S–CH_3), 3.65 (s, 3H, N–CH_3), 5.63 (s, 1H, pyrimidine CH), 9.73 (s, 1H, NH), 10.09 (s, 1H, NH). LC-MS (ESI^+), t_R = 0.513 min: *m*/*z* 240.0 $[M + H]^+$. Anal. calcd for $C_8H_9N_5O_2S$: C, 40.16; H, 3.79; N, 29.27; S, 13.40%. Found: C, 40.07; H, 3.92; N, 29.13; S, 13.54%.

6-(5-(Ethylthio)-4-methyl-4H-1,2,4-triazol-3-yl)pyrimidine-2,4(1H,3H)-dione (**4**). Yield 71%; brown powder; mp 148 °C (MeOH). ^{1}H NMR (500 MHz, DMSO-d_6) δ 1.36 (t, J = 6.1 Hz, 3H, CH_3), 3.08 (q, J = 6.2 Hz, 2H, S–CH_2), 3.68 (s, 3H, N–CH_3), 6.11 (s, 1H, pyrimidine CH), 11.16 (s, 1H, NH), 11.75 (s, 1H, NH). LC-MS (ESI^+), t_R = 0.786 min: *m*/*z* 254.0 $[M + H]^+$. Anal. calcd for $C_9H_{11}N_5O_2S$: C, 42.68; H, 4.38; N, 27.65; S, 12.66%. Found: C, 42.59; H, 4.57; N, 27.58; S, 12.72%.

6-(4-Methyl-5-(propylthio)-4H-1,2,4-triazol-3-yl)pyrimidine-2,4(1H,3H)-dione (**5**). Yield 73%; brown powder; mp 152 °C (MeOH). ^{1}H NMR (500 MHz, DMSO-d_6) δ 1.05 (t, J = 7.0 Hz, 3H, CH_3), 1.76 (q, J = 7.0, 5.3 Hz, 2H, CH_2), 3.10 (t, J = 5.3 Hz, 2H, S–CH_2), 3.68 (s, 3H, N–CH_3), 6.11 (s, 1H, pyrimidine CH), 11.16 (s, 1H, NH), 11.75 (s, 1H, NH). LC-MS (ESI^+), t_R = 0.907 min: *m*/*z* 268.2 $[M + H]^+$. Anal. calcd for $C_{10}H_{13}N_5O_2S$: C, 44.93; H, 4.90; N, 26.20; S, 11.99%. Found: C, 44.88; H, 5.03; N, 26.18; S, 11.92%.

6-(5-(Butylthio)-4-methyl-4H-1,2,4-triazol-3-yl)pyrimidine-2,4(1H,3H)-dione (**6**). Yield 65%; brown powder; mp 155 °C (MeOH). ^{1}H NMR (500 MHz, DMSO-d$_6$) δ 0.92 (t, J = 7.1 Hz, 3H, CH_3), 1.40 (qt, J = 7.1, 6.1 Hz, 2H, CH_2), 1.62–1.71 (m, 2H, CH_2), 3.14 (t, J = 6.7 Hz, 2H, S–CH_2), 3.68 (s, 3H, N–CH3), 6.11 (s, 1H, pyrimidine CH), 11.16 (s, 1H, NH), 11.75 (s, 1H, NH). LC-MS (ESI$^+$), t_R = 0.854 min: m/z 282.2 [M + H]$^+$. Anal. calcd for $C_{11}H_{15}N_5O_2S$: C, 46.96; H, 5.37; N, 24.89; S, 11.40%. Found: C, 46.83; H, 5.52; N, 24.75; S, 11.42%.

6-(4-Methyl-5-(pentylthio)-4H-1,2,4-triazol-3-yl)pyrimidine-2,4(1H,3H)-dione (**7**). Yield 68%; brown powder; mp 166 °C (MeOH). ^{1}H NMR (500 MHz, DMSO-d$_6$) δ 0.84–0.93 (m, 3H, CH_3), 1.33–1.45 (m, 4H, CH_2), 1.68–1.77 (m, 2H, CH_2), 3.12 (t, J = 6.0 Hz, 2H, S–CH_2), 3.68 (s, 3H, N–CH_3), 6.11 (s, 1H, pyrimidine CH), 11.16 (s, 1H, NH), 11.75 (s, 1H, NH). LC-MS (ESI$^+$), t_R = 0.890 min: m/z 296.2 [M + H]$^+$. Anal. calcd for $C_{12}H_{17}N_5O_2S$: C, 48.80; H, 5.80; N, 23.71; S, 10.85%. Found: C, 48.68; H, 5.92; N, 23.62; S, 10.73%.

6-(5-(Hexylthio)-4-methyl-4H-1,2,4-triazol-3-yl)pyrimidine-2,4(1H,3H)-dione (**8**). Yield 58%; brown powder; mp 168 °C (MeOH). ^{1}H NMR (500 MHz, DMSO-d$_6$) δ 0.84–0.92 (m, 3H, CH_3), 1.25–1.42 (m, 6H, CH_2), 1.68 (quint, J = 6.2 Hz, 2H, CH_2), 3.10 (t, J = 6.4 Hz, 2H, S–CH_2), 3.68 (s, 3H, N–CH_3), 6.11 (s, 1H, pyrimidine CH), 11.16 (s, 1H, NH), 11.75 (s, 1H, NH). LC-MS (ESI$^+$), t_R = 0.801 min: m/z 310.2 [M + H]$^+$. Anal. calcd for $C_{13}H_{19}N_5O_2S$: C, 50.47; H, 6.19; N, 22.64; S, 10.36%. Found: C, 50.34; H, 6.34; N, 22.56; S, 10.25%.

6-(5-(Heptylthio)-4-methyl-4H-1,2,4-triazol-3-yl)pyrimidine-2,4(1H,3H)-dione (**9**). Yield 54%; brown powder; mp 175 °C (MeOH). ^{1}H NMR (500 MHz, DMSO-d$_6$) δ 0.84–0.93 (m, 3H, CH_3), 1.21–1.39 (m, 8H, CH_2), 1.68 (quint, J = 6.5 Hz, 2H, CH_2), 3.10 (t, J = 6.4 Hz, 2H, S–CH_2), 3.68 (s, 3H, N–CH_3), 6.11 (s, 1H, pyrimidine CH), 11.16 (s, 1H, NH), 11.75 (s, 1H, NH). LC-MS (ESI$^+$), t_R = 0.872 min: m/z 324.2 [M + H]$^+$. Anal. calcd for $C_{14}H_{21}N_5O_2S$: C, 51.99; H, 6.55; N, 21.65; S, 9.91%. Found: C, 51.78; H, 6.82; N, 21.45; S, 9.82%.

6-(4-Methyl-5-(octylthio)-4H-1,2,4-triazol-3-yl)pyrimidine-2,4(1H,3H)-dione (**10**). Yield 76%; brown powder; mp 182 °C (MeOH). ^{1}H NMR (500 MHz, DMSO-d$_6$) δ 0.83–0.93 (m, 3H, CH_3), 1.21–1.40 (m, 10H, CH_2), 1.68 (quint, J = 6.5 Hz, 2H, CH_2), 3.10 (t, J = 6.4 Hz, 2H, S–CH_2), 3.68 (s, 3H, N–CH_3), 6.11 (s, 1H, pyrimidine CH), 11.16 (s, 1H, NH), 11.75 (s, 1H, NH). LC-MS (ESI$^+$), t_R = 0.907 min: m/z 338.2 [M + H]$^+$. Anal. calcd for $C_{15}H_{23}N_5O_2S$: C, 53.39; H, 6.87; N, 20.75; S, 9.50%. Found: C, 53.23; H, 6.94; N, 20.63; S, 9.42%.

6-(4-Methyl-5-(nonylthio)-4H-1,2,4-triazol-3-yl)pyrimidine-2,4(1H,3H)-dione (**11**). Yield 72%; brown powder; mp 202 °C (MeOH). ^{1}H NMR (500 MHz, DMSO-d$_6$) δ 0.83–0.93 (m, 3H, CH_3), 1.21–1.36 (m, 12H, CH_2), 1.68 (quint, J = 6.5 Hz, 2H, CH_2), 3.10 (t, J = 6.4 Hz, 2H, S–CH_2), 3.68 (s, 3H, N–CH_3), 6.11 (s, 1H, pyrimidine CH), 11.16 (s, 1H, NH), 11.75 (s, 1H, NH). LC-MS (ESI$^+$), t_R = 0.961 min: m/z 352.2 [M + H]$^+$. Anal. calcd for $C_{16}H_{25}N_5O_2S$: C, 54.68; H, 7.17; N, 19.93; S, 9.12%. Found: C, 54.57; H, 7.32; N, 19.82; S, 9.01%.

6-(5-(Decylthio)-4-methyl-4H-1,2,4-triazol-3-yl)pyrimidine-2,4(1H,3H)-dione (**12**). Yield 81%; yellow powder; mp 208 °C (MeOH). ^{1}H NMR (500 MHz, DMSO-d$_6$) δ 0.84–0.93 (m, 3H, CH_3), 1.20–1.36 (m, 14H, CH_2), 1.68 (quint, J = 6.5 Hz, 2H, CH_2), 3.10 (t, J = 6.4 Hz, 2H, S–CH_2), 3.68 (s, 3H, N–CH_3), 6.11 (s, 1H, pyrimidine CH), 11.16 (s, 1H, NH), 11.75 (s, 1H, NH). ^{13}C NMR (125 MHz, DMSO-d$_6$) δ 12.50, 20.64, 22.69, 26.45, 27.03, 27.22, 27.46, 27.68, 29.84, 30.85, 31.06, 93.60, 149.85, 152.32, 154.06, 158.62, 165.19. LC-MS (ESI$^+$), t_R = 0.811 min: m/z 339.8 [M + H]$^+$, 341.8 [M + H + 2]$^+$. Anal. calcd for $C_{17}H_{27}N_5O_2S$: C, 55.87; H, 7.45; N, 19.16; S, 8.77%. Found: C, 55.76; H, 7.84; N, 19.11; S, 8.65%.

Preparation of -((5-(2,6-Dioxo-1,2,3,6-tetrahydropyrimidin-4-yl)-4-methyl-4H-1,2,4-triazol-3-yl)thio)acetic acid (**13**)*:* Compound **2** (5 mmol) and sodium hydroxide (5 mmol) were mixed in propan-2-ol (10 mL), and monochloroacetic acid (5 mmol) was added. The reaction mixture was heated under reflux for 2 h, cooled, diluted with purified water, and

acidified with acetic acid. The precipitated product was collected by filtration, washed with purified water, dried, and recrystallized from water.

2-((5-(2,6-Dioxo-1,2,3,6-tetrahydropyrimidin-4-yl)-4-methyl-4H-1,2,4-triazol-3-yl)thio) acetic acid (**13**). Yield 83%; white powder; mp 238 °C (H_2O). ^{1}H NMR (500 MHz, DMSO-d_6) δ 3.69 (s, 3H, N–CH_3), 4.08 (s, 2H, S–CH_2–COOH), 6.11 (s, 1H, pyrimidine CH), 11.16 (s, 1H, NH), 11.36 (s, 1H, COOH), 11.75 (s, 1H, NH). LC-MS (ESI$^+$), t_R = 0.824 min: *m*/*z* 284.0 [M + H]$^+$. Anal. calcd for $C_9H_9N_5O_4S$: C, 38.16; H, 3.20; N, 24.72; S, 11.32%. Found: C, 38.29; H, 3.52; N, 24.85; S, 11.46%.

Preparation of the morpholinium salt–morpholin-4-ium 2-((5-(2,6-dioxo-1,2,3,6-tetrahydropyrimidin-4-yl)-4-methyl-4H-1,2,4-triazol-3-yl)thio)acetate (**14**): Compound **13** (5 mmol) was suspended in purified water (10 mL), and morpholine (5 mmol) was added. The mixture was stirred at room temperature until a clear homogeneous solution was obtained. The solution was concentrated under reduced pressure, and the product was precipitated by adding diethyl ether (20 mL). The precipitate was collected by filtration, washed with cold diethyl ether (10 mL), and dried to constant mass.

Morpholin-4-ium 2-((5-(2,6-dioxo-1,2,3,6-tetrahydropyrimidin-4-yl)-4-methyl-4H-1,2,4-triazol-3-yl)thio)acetate (**14**). Yield 73%; white powder; mp 211 °C. Anal. calcd for $C_{13}H_{18}N_6O_5S$: C, 42.16; H, 4.90; N, 22.69; S, 8.66%. Found: C, 42.43; H, 4.82; N, 22.85; S, 8.34%.

General procedure for the synthesis of ester derivatives **15**–**18**: A mixture of **2** (5 mmol) and sodium hydroxide (5 mmol) in propan-2-ol (10 mL) was prepared. The corresponding alkyl 2-chloroacetate (5 mmol) was added, and the reaction mixture was heated under reflux for 2 h. After cooling, the precipitate was collected by filtration, washed with purified water, dried, and recrystallized from methanol.

Methyl 2-((5-(2,6-dioxo-1,2,3,6-tetrahydropyrimidin-4-yl)-4-methyl-4H-1,2,4-triazol-3-yl)thio)acetate (**15**). Yield 54%; yellow powder; mp 262 °C (MeOH). ^{1}H NMR (500 MHz, DMSO-d_6) δ 3.69 (s, 3H, N–CH_3), 3.72 (s, 3H, OCH_3), 4.08 (s, 2H, S–CH_2), 6.11 (s, 1H, pyrimidine CH), 11.16 (s, 1H, NH), 11.75 (s, 1H, NH). LC-MS (ESI$^+$), t_R = 0.534 min: *m*/*z* 298.0 [M + H]$^+$. Anal. calcd for $C_{10}H_{11}N_5O_4S$: C, 40.40; H, 3.73; N, 23.56; S, 10.78%. Found: C, 40.29; H, 3.94; N, 23.61; S, 10.89%.

Ethyl 2-((5-(2,6-dioxo-1,2,3,6-tetrahydropyrimidin-4-yl)-4-methyl-4H-1,2,4-triazol-3-yl)thio)acetate (**16**). Yield 73%; yellow powder; mp 268 °C (MeOH). ^{1}H NMR (500 MHz, DMSO-d_6) δ 1.20–1.27 (m, 3H, CH_3), 3.69 (s, 3H, N–CH_3), 4.07 (s, 2H, S–CH_2), 4.16 (q, J = 6.6 Hz, 2H, O–CH_2), 6.11 (s, 1H, pyrimidine CH), 11.16 (s, 1H, NH), 11.75 (s, 1H, NH). LC-MS (ESI$^+$), t_R = 0.641 min: *m*/*z* 312.2 [M + H]$^+$. Anal. calcd for $C_{11}H_{13}N_5O_4S$: C, 42.44; H, 4.21; N, 22.50; S, 10.30%. Found: C, 42.31; H, 4.53; N, 22.42; S, 10.44%.

Isopropyl 2-((5-(2,6-dioxo-1,2,3,6-tetrahydropyrimidin-4-yl)-4-methyl-4H-1,2,4-triazol-3-yl)thio)acetate (**17**). Yield 81%; brown powder; mp 245 °C (MeOH). ^{1}H NMR (500 MHz, DMSO-d_6) δ 1.21 (d, J = 6.0 Hz, 6H, 2CH_3), 3.69 (s, 3H, N–CH_3), 4.07 (s, 2H, S–CH_2), 4.95 (m, 1H, O–CH), 6.11 (s, 1H, pyrimidine CH), 11.16 (s, 1H, NH), 11.75 (s, 1H, NH). LC-MS (ESI$^+$), t_R = 0.842 min: *m*/*z* 326.0 [M + H]$^+$. Anal. calcd for $C_{12}H_{15}N_5O_4S$: C, 44.30; H, 4.65; N, 21.53; S, 9.85%. Found: C, 44.21; H, 4.83; N, 21.47; S, 9.98%.

Butyl 2-((5-(2,6-dioxo-1,2,3,6-tetrahydropyrimidin-4-yl)-4-methyl-4H-1,2,4-triazol-3-yl)thio)acetate (**18**). Yield 87%; brown powder; mp 274 °C (MeOH). ^{1}H NMR (500 MHz, DMSO-d_6) δ 0.92 (t, J = 7.0 Hz, 3H, CH_3), 1.30–1.41 (m, 2H, CH_2), 1.56–1.65 (m, 2H, CH_2), 3.69 (s, 3H, N–CH_3), 4.05–4.11 (m, 4H, S–CH_2 and O–CH_2), 6.11 (s, 1H, pyrimidine CH), 11.16 (s, 1H, NH), 11.75 (s, 1H, NH). ^{13}C NMR (125 MHz, DMSO-d_6) δ 13.78 (C-23), 19.06 (C-22), 30.68 (C-21), 31.15 (C-20), 34.69 (C-15), 64.87 (C-19), 98.32 (C-3), 137.92 (C-4), 150.51 (C-6), 150.91 (C-9), 154.43 (C-12), 165.05 (C-2), 169.49 (C-16). LC-MS (ESI$^+$), t_R = 0.811 min:

m/*z* 339.8 $[M + H]^+$, 341.8 $[M + H + 2]^+$. Anal. calcd for $C_{13}H_{17}N_5O_4S$: C, 46.01; H, 5.05; N, 20.64; S, 9.45%. Found: C, 45.89; H, 5.41; N, 20.56; S, 9.63%.

Preparation of acetamide **19**: A mixture of **2** (5 mmol) and sodium hydroxide (5 mmol) in propan-2-ol (10 mL) was prepared, and 2-chloroacetamide (5 mmol) was added. The reaction mixture was heated under reflux for 2 h and cooled. The precipitated product was collected by filtration, washed with purified water, dried, and recrystallized from *N*,*N*-dimethylformamide.

2-((5-(2,6-Dioxo-1,2,3,6-tetrahydropyrimidin-4-yl)-4-methyl-4H-1,2,4-triazol-3-yl)thio) acetamide (**19**). Yield 83%; white powder; mp 245 °C (DMF). ^{1}H NMR (500 MHz, DMSO-d_6) δ 3.68 (s, 3H, N-CH_3), 4.01 (s, 2H, S-CH_2), 6.11 (s, 1H, pyrimidine CH), 7.05 (s, 2H, NH_2), 11.16 (s, 1H, NH), 11.75 (s, 1H, NH). LC-MS (ESI^+), t_R = 0.955 min: *m*/*z* 283.0 $[M + H]^+$. Anal. calcd for $C_9H_{10}N_6O_3S$: C, 38.30; H, 3.57; N, 29.77; S, 11.36%. Found: C, 38.41; H, 3.77; N, 29.62; S, 11.43%.

In silico prediction of ADME and drug-likeness properties: Prediction of pharmacokinetic parameters and drug-likeness of the studied compounds was performed using the SwissADME web platform (Molecular Modelling Group, Swiss Institute of Bioinformatics, Lausanne, Switzerland; access date: 11 July 2026) [31,32].

Molecular docking: Crystallographic structures of the studied enzymes (1GKC, 1QIB, 4H3X, 7XJO, 8H78) were obtained from the Protein Data Bank [33]. Receptor preparation included removal of cocrystallized ligands, water molecules and minor heteroatoms, addition of polar hydrogen atoms and assignment of partial charges; functionally significant cofactors and catalytic ions, in particular Zn^{2+} in matrix metalloproteinases, were retained. Three-dimensional structures of the compounds were generated from SMILES using RDKit 2026.03.3 (RDKit Project; T5 Informatics GmbH, Basel, Switzerland) and Open Babel 3.1.0. (Open Babel Development Team, University of Pittsburgh, Pittsburgh, PA, USA). Explicit hydrogen atoms were added, followed by geometry optimization and conversion to PDBQT format [34,35]. During structure preparation and file-format conversion, the 1,2,4-triazole ring was represented using explicit single and double bond orders rather than aromatic bond notation. Molecular docking was performed in the smina 2020.12.10 program (University of Pittsburgh, Pittsburgh, PA, USA; based on AutoDock Vina 1.1.2.) [36,37]. The search region was centered on the position of the corresponding cocrystallized ligand. The conformation with the lowest calculated binding energy, the absence of pronounced steric conflicts, and a chemically justified orientation was selected for analysis. The protocol was validated by redocking of cocrystallized ligands; according to the results of the final validation, the RMSD between the experimental and reproduced poses for all enzyme targets was <2.0 Å. Protein–ligand interactions were analyzed using PLIP 3.0.0 (Biotechnology Center, TU Dresden, Dresden, Germany) [38], and complexes were visualized in PyMOL 3.1.0 and Maestro 11.8 (Schrödinger, LLC, New York, NY, USA) [39–41].

For molecular dynamics studies, complexes of MMP-9 with **NNGH**, 13, 17 and 19, as well as the apoform of the enzyme, were selected. The systems were prepared in CHARMM-GUI v3.7 (Lehigh University, Bethlehem, PA, USA) [42] using the CHARMM36m force field for the protein [43] and CGenFF for the ligands [44]. The complexes were solvated with TIP3P water in a periodic cell, neutralized with Na^+/Cl^- ions, and the NaCl concentration was adjusted to 0.15 M. After energy minimization and equilibration, 100 ns productive simulations were performed in GROMACS 2026.2 (GROMACS Development Team, Stockholm, Sweden) [45] at a temperature of 310 K, a pressure of 1 bar, and a time step of 2 fs. The temperature was maintained by a velocity-rescaling thermostat, and the pressure by a C-rescale barostat; electrostatic interactions were calculated by the particle mesh Ewald method, the cutoff radius of nonvalent interactions was 1.2 nm, and bonds involving hydrogen atoms were constrained by the LINCS algorithm. Coordinates were saved every 0.1 ns.

After correction of periodic boundary conditions and alignment of trajectories by Cα atoms, the protein and ligand RMSD, RMSF, radius of gyration, SASA, and hydrogen bonds were estimated. For MMP-9 complexes, the minimum distance between the catalytic Zn^{2+} and the nearest N, O, or S atom of the ligand was additionally determined; values of ≤0.30 nm were considered as direct contact with the metal, and ≤0.50 nm as close proximity to the catalytic ion.

The binding energy of the complexes was estimated by MM-PBSA/MM-GBSA methods in the gmx_MMPBSA 1.6.5 program (University of Medellín, Medellín, Colombia; international open-source development team) [46] along a single trajectory, keeping the catalytic Zn^{2+} in the receptor. For calculations, a final interval of 80–100 ns was used, which included 201 uniformly selected frames. The binding energy was determined as $\Delta G_{bind} = G_{complex} - G_{receptor} - G_{ligand}$, taking into account the van der Waals, electrostatic, polar and non-polar components of solvation. The results were presented as the mean ± standard deviation. The results were graphically presented in GraphPad Prism 10 (GraphPad Software, LLC, Boston, MA, USA).

In vitro MMP-2/MMP-9: The inhibitory activity of the synthesized compounds against matrix metalloproteinases MMP-2 and MMP-9 was determined in vitro by fluorimetric method using SensoLyte® 520 MMP-2 Assay Kit, cat. no. AS-71151, and SensoLyte® 520 MMP-9 Assay Kit, cat. no. AS-71155 (AnaSpec, Fremont, CA, USA) according to the manufacturer's recommendations. The kits contained peptide FRET substrates labeled with the fluorophore 5-FAM and the quencher QXL™520. Proteolytic cleavage of the substrate by the corresponding metalloproteinase was accompanied by the recovery of 5-FAM fluorescence, the intensity of which was proportional to the enzymatic activity.

The test compounds were dissolved in DMSO and added to the reaction mixture to a final concentration of 10 μM. The DMSO content was the same in the test and control wells. **NNGH**, cat. no. SML0584, purity ≥98% by HPLC (Sigma-Aldrich, St. Louis, MO, USA), at a concentration of 10 μM was used as a reference inhibitor.

The assay was performed in black 96-well plates with a flat bottom and a surface with low nonspecific binding. A solution of the corresponding purified recombinant enzyme and the test compound were added to the wells; the total volume was 50 μL. At the same time, an enzyme activity control without inhibitor, a solvent control, a control with **NNGH**, an autofluorescence control of each compound without enzyme, and a substrate control were prepared. When using enzyme proforms, they were pre-activated with 1 mM 4-aminophenylmercury acetate: pro-MMP-2 for 1 h, and pro-MMP-9 for 2 h at 37 °C. The recombinant catalytic domain of MMP-9 did not require additional activation.

After pre-incubation of the enzyme with the compound for 10–15 min, 50 μL of the corresponding FRET substrate, previously diluted 1:100 with kit buffer, was added to each well. The total volume of the reaction mixture was 100 μL. The fluorescence intensity was recorded at excitation and emission wavelengths of 490 and 520 nm, respectively, every 5 min for 30–60 min using an Agilent Cary Eclipse spectrofluorimeter equipped with a Cary Eclipse Microplate Reader module (Agilent Technologies, Santa Clara, CA, USA).

The initial reaction rate was determined by the slope of the linear plot of fluorescence intensity versus time after subtracting the corresponding background signal. The percentage of inhibition was calculated by the formula:

$$Inhibition,\ \% = \left(1 - \frac{V_{test}}{V_{control}}\right) \times 100\%,$$

where V_{test} is the background-corrected reaction rate in the presence of the test compound, and $V_{control}$ is the background-corrected reaction rate in the solvent control.

3. Results

The target compound 2, which combines the pyrimidine-2,4-dione core of orotic acid and a 4-methyl-1,2,4-triazole-3-thiol fragment, was obtained by sequential formation of a triazole ring from orotic acid hydrazide (Figure 2). In the first stage, the nucleophilic addition of the terminal NH_2 group of the hydrazide to methyl isothiocyanate occurred with the formation of the corresponding *N*-acylthiosemicarbazide. The reaction was carried out in propan-2-ol under moderate heating; the formed intermediate product precipitated, which made it possible to isolate it by filtration without the use of column chromatography.

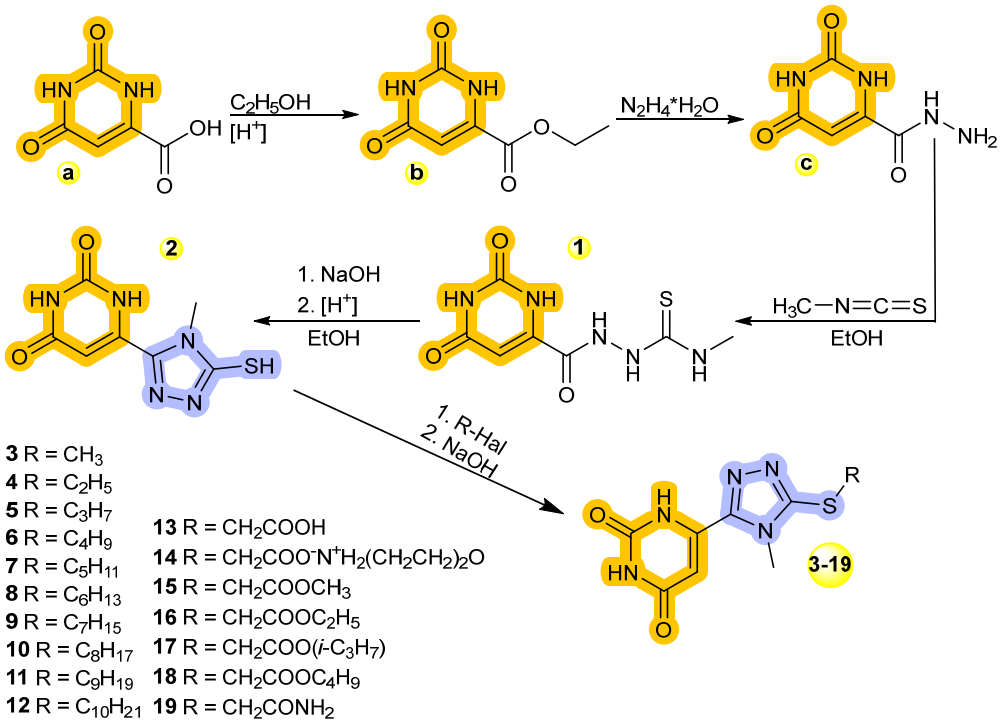

Figure 2. Scheme of the synthesis of hybrid derivatives combining the orotic acid (pyrimidine-2,4-dione) core and the 4-methyl-1,2,4-triazole fragment.

Subsequent alkaline cyclocondensation of the carbothioamide led to the closure of the 1,2,4-triazole ring and the formation of **2**. After cooling and acidification of the reaction mixture with acetic acid, the target product was precipitated as a light-yellow powder in 64% yield. Compound **2** is characterized by thione-thiol tautomerism: in neutral medium, the compound can exist predominantly in the thione form, while in alkaline medium, deprotonation of the mercapto group leads to the formation of a reactive thiolate anion [47].

The sulfur atom was functionalized by selective S-alkylation of **2** with the corresponding alkyl halides in the presence of an equimolar amount of sodium hydroxide in propan-2-ol. The result was a homologous series **3**–**12** with methyl, ethyl, propyl, butyl, pentyl, hexyl, heptyl, octyl, nonyl, and decyl substituents. The product yields were 54–81%. Under the conditions used, S-alkylation predominated, while competitive alkylation of the nitrogen atoms of the triazole or pyrimidine rings was not observed. The functionalized carboxymethyl moiety was introduced by a similar nucleophilic substitution reaction. The interaction of **2** with monochloroacetic acid led to the formation of the carboxylic acid **13**, which was further converted into the morpholinium salt **14**. Reactions of **2** with the corresponding alkyl esters of monochloroacetic acid gave the methyl, ethyl, isopropyl, and butyl esters **15**–**18**. The use of 2-chloroacetamide provided the amide derivative **19**.

The structure of the synthesized compounds was confirmed by the results of ^{1}H and in some cases ^{13}C NMR spectroscopy, mass spectrometry and elemental analysis. In the

spectrum of **2**, an SH-proton signal was observed at 7.01 m.p., which disappeared after S-alkylation. For **3**, a characteristic S–CH_3 signal appeared at 2.62 m.p., while for higher homologues, S–CH_2 signals were recorded at approximately 3.10–3.14 m.p. In the mass spectra of the **3**–**12** series, the $[M + H]^+$ values increased regularly from m/z 240 to 366 with a step of 14 Da, which corresponded to the sequential elongation of the alkyl chain by one methylene group.

For **13** and derivatives **15**–**19**, the singlet of the methylene group S–CH_2–CO at 4.01–4.08 ppm was characteristic. In the spectrum of the acid **13**, a COOH signal was additionally observed at 11.36 ppm, in the esters the corresponding signals of O-alkyl groups, and in the amide **19** an NH_2 signal at 7.05 ppm. The preservation of the signals of the pyrimidine ring proton and two imide NH protons confirmed that the S-functionalization occurred without disrupting the 1,2,4-triazole–pyrimidine-2,4-dione skeleton.

The predicted ADME/drug-likeness profile of the synthesized 1,2,4-triazole derivatives indicated generally favorable physicochemical characteristics of the series (Table 1). The molecular weight of the compounds was in the range of 225.23–365.49 g/mol, which corresponds to the typical range for low molecular weight biologically active substances. The consensus LogP values varied from −1.33 to 3.13, indicating moderate lipophilicity of most compounds. For alkylthio derivatives **3**–**12**, a regular increase in molecular weight, number of rotational bonds, molar refraction, Fsp^3, and LogP with increasing alkyl fragment length was observed. At the same time, a gradual decrease in the calculated aqueous solubility was observed for this subseries, which is an expected consequence of the increase in hydrophobicity of the molecules.

Table 1. Predicted ADME/drug-likeness profile of 1,2,4-triazole derivatives.

Comp	MW	Fsp^3	HBA/HBD	MR	TPSA, Å^2	LogP	LogS	Solubility, mg/mL	log Kp, cm/s	Bioavailability Score	SA
2	225.23	0.14	4/2	55.21	135.23	−0.65	−2.54	0.652	−6.74	0.55	2.40
3	239.25	0.25	4/2	59.68	121.73	−0.31	−2.75	0.423	−6.57	0.55	2.64
4	253.28	0.33	4/2	64.49	121.73	0.04	−2.97	0.271	−6.40	0.55	2.81
5	267.31	0.40	4/2	69.30	121.73	0.43	−3.30	0.134	−6.11	0.55	3.00
6	281.33	0.45	4/2	74.10	121.73	0.77	−3.52	0.085	−5.94	0.55	3.10
7	295.36	0.50	4/2	78.91	121.73	1.17	−3.86	0.041	−5.65	0.55	3.21
8	309.39	0.54	4/2	83.72	121.73	1.56	−4.20	0.019	−5.35	0.55	3.31
9	323.41	0.57	4/2	88.52	121.73	1.95	−4.55	0.009	−5.05	0.55	3.42
10	337.44	0.60	4/2	93.33	121.73	2.34	−4.89	0.004	−4.75	0.55	3.53
11	351.47	0.62	4/2	98.14	121.73	2.74	−5.24	0.002	−4.45	0.55	3.64
12	365.49	0.65	4/2	102.95	121.73	3.13	−5.59	0.001	−4.15	0.55	3.76
13	283.26	0.22	6/3	66.26	159.03	−0.85	−2.55	0.790	−7.13	0.11	2.90
14	283.26	0.22	6/3	66.26	159.03	−0.85	−2.55	0.790	−7.13	0.11	2.90
15	297.29	0.30	6/2	70.58	148.03	−0.55	−2.76	0.514	−6.98	0.55	2.99
16	311.32	0.36	6/2	75.39	148.03	−0.21	−2.99	0.318	−6.81	0.55	3.13
17	325.34	0.42	6/2	80.20	148.03	0.12	−3.34	0.150	−6.59	0.55	3.23
18	339.37	0.46	6/2	85.00	148.03	0.53	−3.56	0.094	−6.35	0.55	3.32
19	282.28	0.22	5/3	67.40	164.82	−1.33	−2.14	2.050	−7.59	0.55	2.86

Note: MW—molecular weight; HA—heavy atoms; Fsp^3—fraction of sp^3-hybridized carbons; HBA/HBD—hydrogen-bond acceptors/donors; MR—molar refractivity; TPSA—topological polar surface area; LogP—lipophilicity; ESOL LogS—predicted aqueous solubility; log Kp—skin permeation coefficient; SA—synthetic accessibility.

Compounds **13**, **17** and **19**, which were selected as promising MMP inhibitors, were characterized by increased TPSA values of 159.03, 148.03 and 164.82 Å^2, respectively, indicating higher polarity compared to alkylthio derivatives **3**–**12**. Such a profile may limit their systemic absorption, but is acceptable for further consideration in the context of potential topical application, in particular for wound healing activity. Among the active candidates, **17** demonstrated the most balanced combination of molecular weight, polarity, lipophilicity, solubility, bioavailability score and synthetic accessibility, which allows us to consider it as one of the most promising representatives of the series for further in vitro and in vivo studies. All compounds met the Lipinski rule without violations, had no PAINS alerts, were not predicted as BBB-permeant and P-gp substrates; high levels of gastrointestinal absorption were characteristic of **3**–**12**, while **2** and **13**–**19** had low predicted GI absorption.

All compounds fit Lipinski's rule without violations, did not show PAINS alerts, and were predicted as BBB-permeable, non-P-gp substrates; **3**–**12** were predicted to have high gastrointestinal absorption, while **2** and **13**–**19** demonstrated low gastrointestinal absorption.

Molecular docking: To preliminarily determine the potential affinity of the synthesized compounds to biological targets, comparative molecular docking of a series of 1,2,4-triazole derivatives was performed with respect to five enzymatic targets represented by PDB codes 1GKC, 1QIB, 4H3X, 7XJO, and 8H78. **NNGH** was used as a reference compound, which allowed us to estimate not only the absolute values of binding energy, but also the relative advantage of each studied molecule compared to the standard inhibitor.

The docking results (Table 2) were evaluated by the calculated binding energy, or docking affinity, expressed in kcal/mol. More negative affinity values were considered as an indicator of more favorable formation of the "ligand–enzyme" complex. For comparison with the reference compound, the difference ΔG vs **NNGH** was additionally calculated, which was defined as the difference between the affinity of the studied compound and the affinity of **NNGH** for the corresponding enzyme. A negative value of ΔG vs **NNGH** indicated a more favorable, compared to **NNGH**, calculated interaction with the active site of the enzyme.

Overall, the results showed that the affinity of the studied 1,2,4-triazole derivatives significantly depended on the type of enzymatic target. The most pronounced differences between the compounds were observed for the targets 4H3X, 7XJO and 8H78, while for 1QIB the reference compound **NNGH** remained the most effective in terms of docking affinity. Such a distribution may indicate a different correspondence of the spatial structure of the 1,2,4-triazole derivatives to the geometry of the active centers of individual enzymes.

For the 1GKC target, the best results among the studied compounds were demonstrated by **13** and **7**, for which the calculated affinity values were −7.76 and −7.62 kcal/mol, respectively. Both compounds exceeded the reference **NNGH**, whose affinity for this target was −7.43 kcal/mol. The difference relative to **NNGH** was −0.33 kcal/mol for **13** and −0.19 kcal/mol for **7**. Other compounds, in particular **6** and **12**, demonstrated values close to the reference, but did not exceed it in calculated affinity.

For the 1QIB enzyme, the situation was the opposite: **NNGH** had the best affinity of all the molecules analyzed, which was −7.41 kcal/mol. The closest to the reference were **8**, **19**, **11** and **12**, for which the affinity values were −7.26, −7.19, −7.16 and −7.12 kcal/mol, respectively. However, none of the 1,2,4-triazole derivatives outperformed **NNGH** for this target. This may indicate a more optimal correspondence of the **NNGH** structure to the 1QIB active site or a less favorable orientation of the studied 1,2,4-triazole derivatives in the corresponding binding site.

Table 2. Heatmap overview of the most promising derivatives according to molecular docking results.

Compound	1GKC	1QIB	4H3X	7XJO	8H78
2	−5.65	−6.21	−7.91	−5.68	−5.51
3	−5.92	−5.50	−6.24	−5.68	−5.99
4	−5.48	−5.24	−5.92	−5.39	−5.68
5	−5.32	−6.02	−6.38	−5.61	−5.50
6	−7.35	−6.36	−8.71	−8.11	−7.55
7	−7.62	−6.90	−8.77	−7.08	−6.29
8	−6.91	−7.26	−8.69	−7.56	−6.86
9	−6.84	−6.33	−8.72	−7.73	−7.16
10	−7.15	−6.69	−8.25	−7.43	−6.91
11	−7.08	−7.16	−8.76	−6.56	−6.99
12	−7.34	−7.12	−7.34	−5.66	−6.68
13	−7.76	−6.85	−9.17	−7.73	−7.07
14	−7.17	−7.11	−9.44	−6.94	−6.56
15	−7.26	−6.10	−8.93	−7.22	−7.84
16	−6.40	−6.69	−8.97	−6.31	−7.08
17	−6.79	−6.52	−9.65	−8.30	−7.23
18	−6.84	−7.12	−9.26	−7.47	−7.09
19	−7.13	−7.19	−9.47	−8.11	−8.25
NNGH	**−7.43**	**−7.41**	**−8.37**	**−7.05**	**−6.96**

Note: Background colors indicate relative docking affinity: green represents more negative and therefore more favorable binding-energy values, yellow indicates intermediate values, and orange represents less favorable values. **NNGH** is shown without color shading as the reference inhibitor.

The most pronounced results were obtained for the 4H3X target. For this enzyme, most of the selected 1,2,4-triazole derivatives had better affinity values compared to **NNGH**. The reference compound was characterized by an index of −8.37 kcal/mol, while the best compound of the series, **17**, had an affinity of −9.65 kcal/mol, which is 1.28 kcal/mol better than **NNGH**. Also, high results were demonstrated by **19** with an affinity of −9.47 kcal/mol, 14 with an affinity of −9.44 kcal/mol, **18** with an affinity of −9.26 kcal/mol, and **13** with an affinity of −9.17 kcal/mol. Thus, the 4H3X target turned out to be the most sensitive to the structural features of the studied series and gave the widest set of potentially active candidates.

For the 7XJO target, a number of compounds were also found that exceeded the **NNGH** reference. The affinity value of **NNGH** for this enzyme was −7.05 kcal/mol. The most pronounced affinity was shown by 17 with an affinity of −8.30 kcal/mol, which corresponded to an improvement of 1.24 kcal/mol compared to **NNGH**. Next in efficiency were **6** and **19**, which had almost the same affinity indicators about −8.11 kcal/mol. Also, high results were characteristic of **13** and **9**, whose affinity values were approximately −7.73 kcal/mol. Therefore, for 7XJO, **17**, **6**, **19**, **13** and **9** can be considered the most promising.

For the target 8H78, the best among the studied compounds was **19**, whose affinity was −8.25 kcal/mol, while **NNGH** had an index of −6.96 kcal/mol. The difference between **19** and **NNGH** was −1.29 kcal/mol, which is the most pronounced improvement among the results for this target. Also of considerable interest are **15** with an affinity of −7.84 kcal/mol, **6** with an affinity of −7.55 kcal/mol, **17** with an affinity of −7.23 kcal/mol, and **9** with an affinity of −7.16 kcal/mol. The obtained data indicate that for 8H78 the most favorable structural variants are represented by compounds **19**, **15** and **6**.

A generalized analysis of all five enzymes allowed us to identify compounds with the best balance between the calculated binding strength and the stability of the advantage over **NNGH**. The most promising was **13**, which exceeded **NNGH** in four out of five enzymatic targets: 1GKC, 4H3X, 7XJO and 8H78. Its average affinity value for all targets was −7.71 kcal/mol, and the best indicator was obtained for 4H3X −9.17 kcal/mol. Such stability of the results allows us to consider **13** as a priority compound for further in-depth in silico and experimental studies. The promising group also includes **19**, **17**, **6**, **18**, **15**, **9** and **7**, each of which exceeded **NNGH** in three out of five studied targets. Among them, **19** should be especially noted, which had the best average affinity among the entire series at −8.03 kcal/mol, and also demonstrated high values for 4H3X, 7XJO and 8H78. For **17**, the lowest absolute affinity value in the entire array of results was −9.65 kcal/mol, obtained for 4H3X, indicating a potentially very favorable complex formation with this target. However, **17** was less stable compared to **13** in the number of targets where it exceeded **NNGH**. Compounds **8**, **11** and **16** can be considered conditionally promising, as they exceeded **NNGH** in two enzymatic targets. Compounds **14** and **10** showed an advantage for only one target, but individual values, in particular the affinity of **14** for 4H3X at the level of −9.44 kcal/mol, indicate a possible selectivity for a certain type of active site. In contrast, **2**, **3**, **4**, **5** and **12** did not exceed **NNGH** in any of the five targets, so they can be considered as lower priority for further research within this series. Thus, the results of molecular docking indicate that the studied series of 1,2,4-triazole derivatives contains several promising molecules capable of forming more energetically favorable complexes with individual enzymatic targets compared to the reference inhibitor **NNGH**. The most balanced candidate is **13**, which demonstrated superiority over **NNGH** in the largest number of targets. At the same time, **19** and **17** were characterized by the most pronounced absolute affinity values for individual enzymes, which makes them important candidates for further analysis.

For a more detailed interpretation of the molecular docking results of the three most promising compounds, **13**, **19** and **17,** an analysis of non-covalent interactions in complexes with the enzyme 4H3X was carried out using PLIP. This target was chosen for in-depth analysis, since, for it, the studied 1,2,4-triazole derivatives demonstrated the best docking affinity values compared to the reference compound **NNGH**. For the complexes **13**, **19** and **17,** the affinity values were −9.17, −9.47 and −9.65 kcal/mol, respectively, which indicates an energetically favorable formation of the ligand-enzyme complexes.

PLIP analysis (Table 3) showed that the stabilization of the studied ligands in the 4H3X binding site is provided mainly by a system of hydrogen bonds with residues Gly186, Leu188, Ala189, His226, His236, Ala242, Leu243, Met247, Tyr248 and Arg249, and for **17**, hydrophobic contacts with Leu243 and Pro255 were additionally found. A special role in the formation of complexes is probably played by residues His226 and Tyr248, which are repeated in all three complexes and can be considered as key amino acid residues for stabilizing the position of 1,2,4-triazole derivatives within the active center.

The largest number of hydrogen bonds was identified for **13**—10 contacts (Figure 3). The ligand interacts with residues Gly186, Leu188, Ala189, His226, His236, Tyr248 and Arg249. The shortest and geometrically favorable hydrogen bonds are formed with Leu188 with a H–A distance of 2.00 Å and D–A of 2.91 Å, as well as with His226 with a H–A distance of 2.03 Å and D–A of 3.00 Å. Interactions with Tyr248 are represented by three contacts, which indicates the important role of this residue in the orientation of the ligand. Additionally, **13** forms two hydrogen bonds with Arg249, which may provide polar anchoring of the molecule in a peripheral or functionally significant region of the active site. Despite the high number of hydrogen bonds, no hydrophobic contacts were recorded for **13** in the PLIP report, which may partially explain the lower affinity value compared to **19** and **17**.

Table 3. PLIP analysis of non-covalent interactions of selected 1,2,4-triazole derivatives with 4H3X.

Interaction Type	Residue, Chain A	Distance, Å	Angle, °	Interpretation
		13 (Docking affinity = −9.17 kcal/mol)		
H. bond	Gly186	H–A 2.99; D–A 3.94	165.18	Additional polar stabilization near the binding site entrance
H. bond	Leu188	H–A 2.00; D–A 2.91	152.73	Short and geometrically favorable H-bond
H. bond	Ala189	H–A 2.61; D–A 3.27	121.87	Auxiliary polar contact
H. bond	His226	H–A 2.03; D–A 3.00	154.15	Key stabilizing interaction with histidine residue
H. bond	His236	H–A 2.65; D–A 3.53	150.55	Additional interaction with histidine-containing region
H. bond	Tyr248	H–A 2.88–3.17; D–A 3.43–3.80	101.67–150.90	Recurrent contact cluster contributing to ligand orientation
H. bond	Arg249	H–A 2.54–2.77; D–A 3.37–3.69	137.92–155.31	Polar anchoring of the ligand near positively charged residue
		19 (Docking affinity = −9.47 kcal/mol)		
H. bond	Gly186	H–A 3.13; D–A 3.91	139.20	Auxiliary polar interaction
H. bond	His226	H–A 2.35; D–A 3.32	154.35	Conserved interaction also observed for 13 and 17
H. bond	Ala242	H–A 2.12; D–A 3.15	168.57	Highly favorable linear H-bond geometry
H. bond	Leu243	H–A 2.61; D–A 3.49	144.51	Contact with the Leu243 region of the active site
H. bond	Met247	H–A 2.38; D–A 3.31	161.41	Favorable polar contact with Met247
H. bond	Tyr248	H–A 2.97–3.14; D–A 3.89	131.42–150.18	Stabilization through recurrent Tyr248 interaction
		17 (Docking affinity = −9.65 kcal/mol)		
Hydrophobic interaction	Leu243	3.62	—	Hydrophobic stabilization in the binding pocket
	Pro255	3.72	—	Additional hydrophobic contact supporting ligand fitting
H. bond	His226	H–A 2.32–3.21; D–A 3.21–3.90	103.37–141.83	Major interaction cluster with histidine residue
H. bond	Leu243	H–A 2.66; D–A 3.42	131.50	Combined polar/hydrophobic involvement of Leu243 region
H. bond	Met247	H–A 2.22–2.29; D–A 3.23	153.20–171.12	Strong and geometrically favorable interaction pair
H. bond	Tyr248	H–A 3.15–3.34; D–A 3.82–3.98	121.87–124.09	Recurrent stabilizing contact with Tyr248
H. bond	Arg249	H–A 1.93; D–A 2.81	147.89	Strong short polar contact, likely important for anchoring

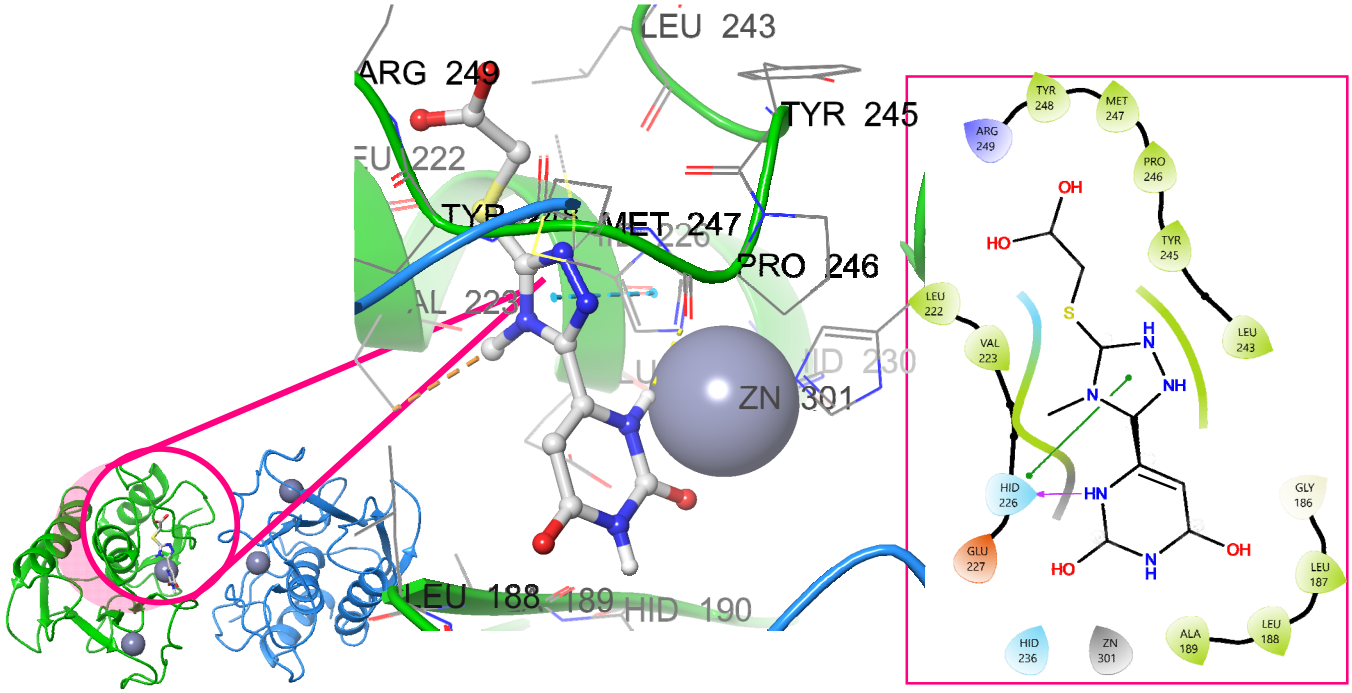

Figure 3. PLIP interaction profile of compound **13** with MMP-9 (PDB ID: 4H3X).

For **17** (Figure 4), which demonstrated the best docking affinity among the three selected compounds, PLIP identified nine hydrogen bonds and two hydrophobic interactions. Hydrogen bonds are formed with residues His226, Leu243, Met247, Tyr248 and Arg249. The most important feature of this complex is the presence of three contacts with His226, which indicates an intense polar interaction of the ligand with this site of the active site. In addition, **17** forms two hydrogen bonds with Met247 and two contacts with Tyr248, which further stabilizes the orientation of the molecule. Of particular importance is the short hydrogen bond with Arg249, for which the H–A distance is 1.93 Å and the D–A distance is 2.81 Å, which may indicate a strong polar anchoring of the ligand. Unlike 13 and **19**, hydrophobic interactions with Leu243 and Pro255 at distances of 3.62 Å and 3.72 Å, respectively, were also recorded for **17**. The combination of a branched hydrogen bond network with hydrophobic contacts may be one of the reasons for the best docking affinity value for **17**.

For **19** (Figure 5), seven hydrogen bonds were found with residues Gly186, His226, Ala242, Leu243, Met247 and Tyr248. Compared to **13**, this compound has a smaller number of polar contacts, but its docking affinity is better, which may indicate a more optimal spatial arrangement of the ligand in the active center of 4H3X. The most favorable contacts in terms of geometry are with Ala242 with a H–A distance of 2.12 Å, D–A 3.15 Å and an angle of 168.57°, as well as with Met247 with a H–A distance of 2.38 Å, D–A 3.31 Å and an angle of 161.41°. The presence of interactions with Leu243, Met247 and Tyr248 indicates that 19 is immersed in the active site, which partially overlaps with the contact zone of **17**. The His226 residue, as in the case of **13**, participates in the formation of a hydrogen bond, which confirms its importance as one of the key stabilizing centers.

The generalization of the interactions shows that all three compounds have a common contact with His226 and Tyr248, which allows us to consider these residues as key for the binding of 1,2,4-triazole derivatives within the active site of 4H3X. Interactions with Arg249 are characteristic of **13** and **17** and may play a role in additional polar anchoring of the ligand. Residues Leu243 and Met247 participate in the stabilization of **19** and **17**, while for 17 Leu243 additionally forms a hydrophobic contact. It is the combination of several hydrogen bonds

with His226, Met247, Tyr248 and Arg249, as well as hydrophobic contacts with Leu243 and Pro255, which probably provides the most favorable position of **17** in the active site and explains its lowest docking affinity value among the studied candidates. Therefore, the results of PLIP analysis are consistent with the molecular docking data and confirm the feasibility of choosing **13**, **19** and **17** as priority candidates for further study. Compound **13** is characterized by the most extensive hydrogen bond network, **19** demonstrates the optimal geometry of individual polar contacts, and **17** combines a pronounced hydrogen bond system with hydrophobic stabilization, which makes it the most promising candidate for further molecular dynamics modeling and experimental validation.

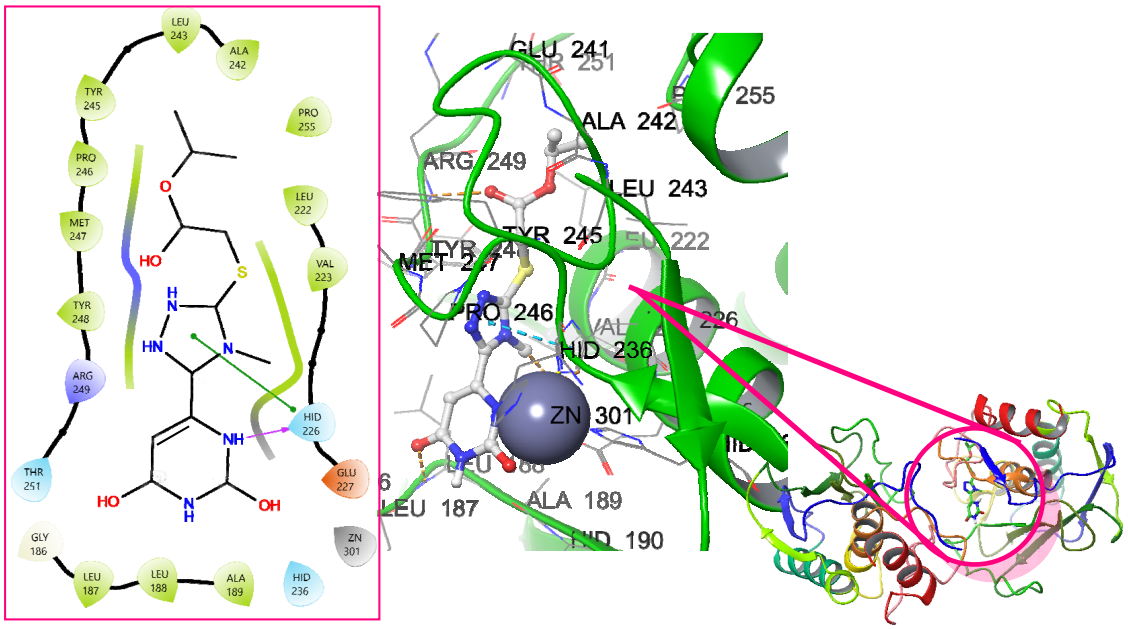

Figure 4. PLIP interaction profile of compound **17** with MMP-9 (PDB ID: 4H3X).

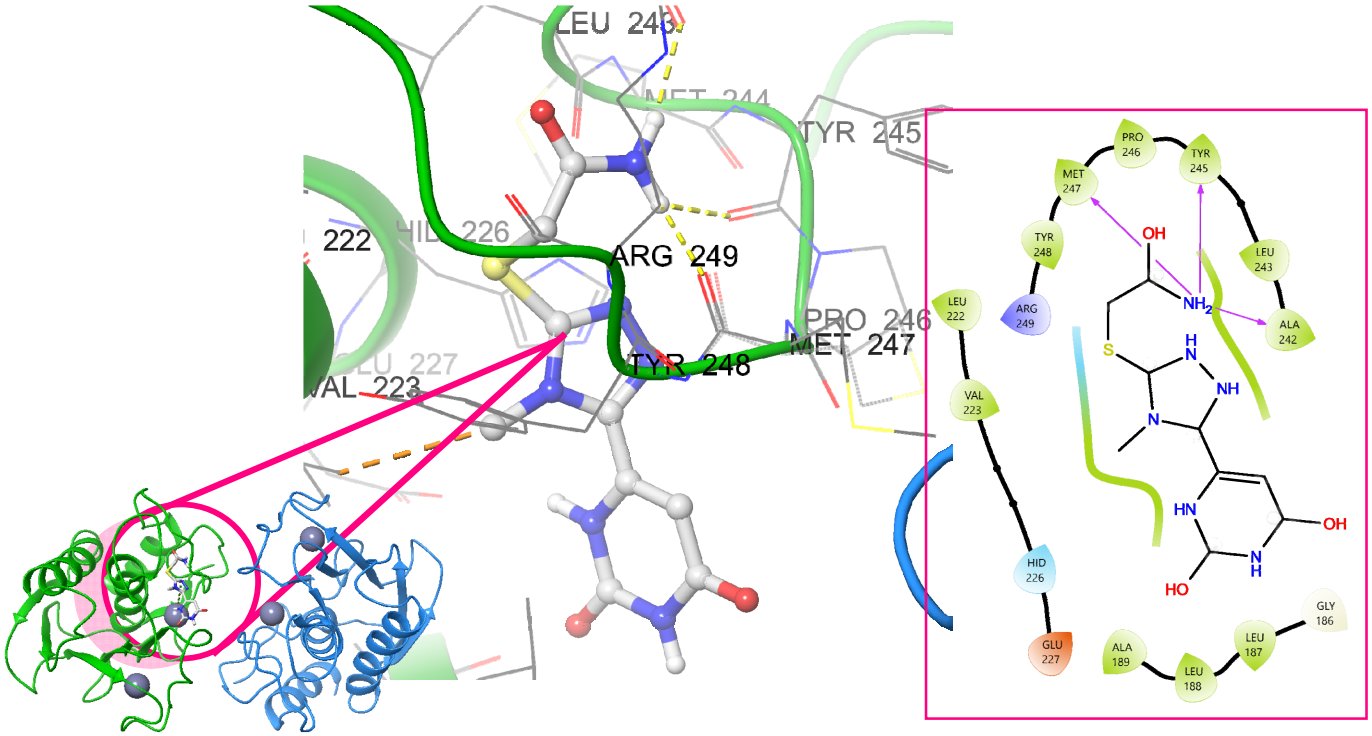

Figure 5. PLIP interaction profile of compound **19** with MMP-9 (PDB ID: 4H3X).

In the context of molecular dynamics, the time dependences of the RMSD of the heavy atoms of the ligands demonstrated significant differences in the ability of the studied compounds to maintain the initial docked pose in the active site of MMP-9 (Figure 6).

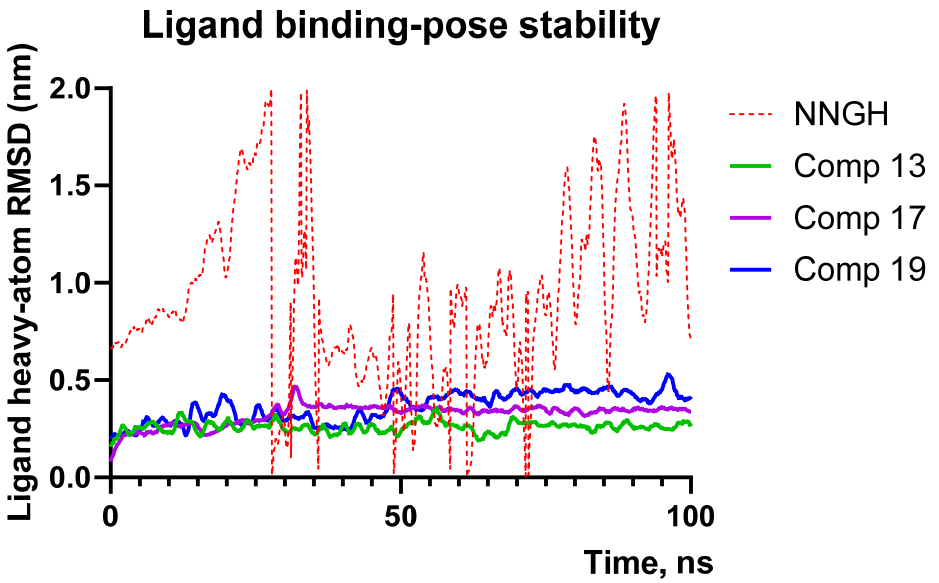

Figure 6. Dynamic stability of bound ligand conformations in complexes with MMP-9 during 100 ns molecular dynamics simulation.

The most stable profile was observed for **13**. After a short initial adaptation period, the ligand RMSD values mainly remained within the range of approximately 0.20–0.30 nm throughout the entire trajectory. In the final interval of 80–100 ns, the median RMSD value for **13** was 0.261 nm, which was the lowest among the studied 1,2,4-triazole derivatives. The obtained result indicates a good preservation of the initial orientation of 13 in the catalytic pocket of MMP-9. For **17**, a moderate increase in RMSD was observed during the first approximately 30 ns, followed by stabilization at a level of about 0.34–0.37 nm. The median ligand RMSD value during 80–100 ns was 0.347 nm. This profile indicates a partial rearrangement of the initial docked pose with subsequent formation of a relatively stable bound conformation. Thus, **17** remained in the active pocket, although its equilibrium orientation differed from the initial docked structure. Compound **19** was characterized by more pronounced conformational mobility. The RMSD values gradually increased and, in the second half of the trajectory, were mainly in the range of 0.40–0.50 nm. The median value for the interval 80–100 ns was 0.433 nm. Compared with **13** and **17**, this indicates a less rigid retention of the initial conformation and a greater mobility of **19** in the middle of the binding pocket. A fundamentally different profile was found for **NNGH**. After approximately 25–35 ns, a sharp increase in ligand RMSD to several nanometers was observed. This increase in magnitude indicates the distance of **NNGH** from the initial binding site.

Analysis of the minimum distance between the potentially coordinating heteroatoms of the ligands and the Zn^{2+} catalyst ion confirmed the most favorable profile for **13** (Figure 7). Throughout almost the entire 100 ns trajectory, the distance remained close to 0.21 nm, i.e., approximately 2.1 Å, and did not exceed the selected direct contact criterion of 0.30 nm. In the final interval of 80–100 ns, the median distance was 0.211 nm. This indicates a stable retention of the potentially coordinating group of **13** directly near the catalyst metal.

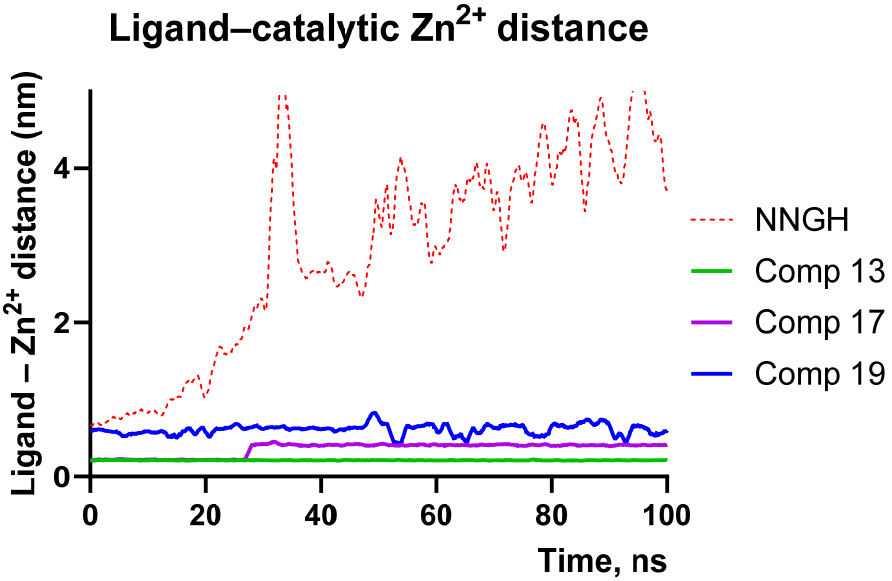

Figure 7. Dynamics of ligand positioning relative to the catalytic Zn^{2+} ion in complexes with MMP-9 during 100 ns molecular dynamics simulation.

For 17, the distance to Zn^{2+} was also about 0.21–0.23 nm for the initial approximately 28 ns. After that, there was a jump in the distance to about 0.40–0.42 nm, which remained stable until the end of the simulation. The median distance over 80–100 ns was 0.409 nm. Thus, **17** lost direct coordination to Zn^{2+}, but remained within 5 Å of the catalyst ion. This is consistent with a transition from the primary metal-coordinating pose to another stable orientation, which may be maintained by contacts with amino acid residues in the active pocket. Compound **19** was approximately 0.50–0.70 nm from the catalytic Zn^{2+} for most of the trajectory, although there were some short-term approaches to the 0.50 nm limit. The median distance in the final interval was 0.653 nm. Thus, the stabilization of **19** is likely determined mainly by interactions with amino acid residues in the peripheral part of the active pocket, rather than by direct coordination of the catalytic metal. For **NNGH**, the distance to Zn^{2+} gradually increased already in the first third of the trajectory, and after about 30 ns it reached several nanometers. In the final interval, the median distance was 4.385 nm. This confirms the conclusion obtained from the ligand RMSD that **NNGH** lost its initial pose in the active site within this trajectory.

The combined analysis of the two time parameters allowed us to establish the following order of dynamic stability of the complexes: **13** > **17** > **19** >> **NNGH**. Compound **13** was simultaneously characterized by the lowest ligand RMSD and a stable close distance to the catalytic Zn^{2+}, which makes it the most convincing candidate according to the results of MD-validation docking. Compound **17** demonstrated stable retention in the active pocket after restructuring the initial pose, while **19** was retained mainly in the peripheral part of the catalytic center without stable metal coordination.

MM/PBSA calculations were performed for MMP-9 complexes using conformations obtained from the 80–100 ns molecular dynamics interval (Table 4). For all studied complexes, average binding energy values (ΔG_{bind}) were determined, as well as individual energy contributions that shape the overall stability of the complex.

Among the studied compounds, **17** demonstrated the most favorable calculated value of the binding energy with MMP-9, with $\Delta G_{bind} = -26.16 \pm 5.17$ kcal·mol^{-1} (Figure 8). The main contribution to the stabilization of this complex was provided by van der Waals interactions ($\Delta E_{vdW} = -51.95 \pm 2.90$ kcal·mol^{-1}), which indicates a high steric complementarity of the ligand to the active site of the enzyme and the formation of a significant number of non-covalent contacts.

Table 4. MM/PBSA energy components for the investigated MMP-9–inhibitor complexes (mean ± SD in kcal·mol^{-1}).

Energy Component	NNGH	13	17	19
ΔE_{vdW}	−20.78 ± 3.27	−28.51 ± 3.69	−51.95 ± 2.90	−34.96 ± 3.06
ΔE_{ele}	−5.62 ± 6.43	−42.16 ± 4.85	−22.23 ± 4.27	+3.37 ± 4.13
ΔG_{gas}	−26.40 ± 7.16	−70.67 ± 4.01	−74.19 ± 4.34	−31.60 ± 5.37
ΔG_{PB}	+12.23 ± 5.25	+36.92 ± 3.18	+25.53 ± 4.02	+19.63 ± 9.82
$\Delta G_{nonpolar}$	+11.20 ± 1.17	+18.71 ± 1.17	+22.49 ± 1.07	+21.51 ± 1.42
ΔG_{solv}	+23.43 ± 4.87	+55.63 ± 3.61	+48.02 ± 4.49	+41.14 ± 10.80
ΔG_{bind}	−2.98 ± 4.07	−15.04 ± 4.22	−26.16 ± 5.17	+9.54 ± 7.66

Note: ΔE_{vdW} represents the van der Waals interaction energy between the protein and ligand; ΔE_{ele} is the electrostatic interaction energy; ΔG_{gas} is the gas-phase molecular-mechanics contribution calculated as $\Delta E_{vdW} + \Delta E_{ele}$; ΔG_{PB} represents the polar solvation contribution calculated using the Poisson–Boltzmann model; $\Delta G_{nonpolar}$ is the non-polar solvation contribution, including solvent-accessible surface-area-dependent and dispersion terms; ΔG_{solv} is the total solvation contribution calculated as $\Delta G_{PB} + \Delta G_{nonpolar}$; and ΔG_{bind} is the total MM/PBSA binding-energy estimate calculated as $\Delta G_{gas} + \Delta G_{solv}$.

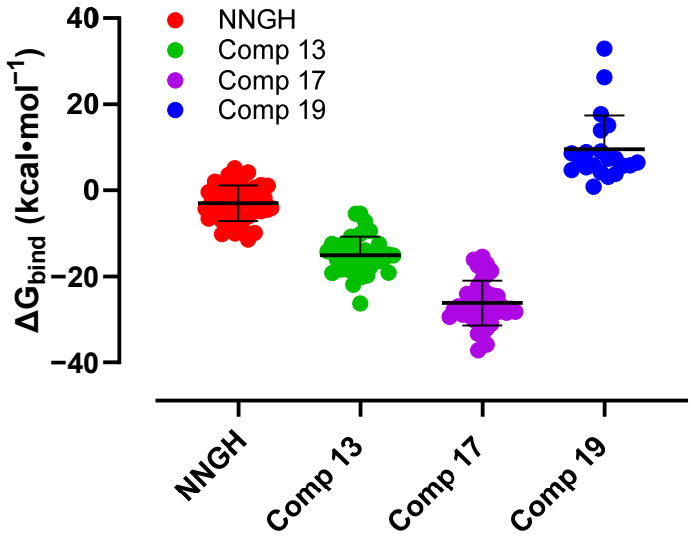

Figure 8. Distribution of frame-by-frame ΔG_{bind} values for MMP-9 complexes in the time interval 80–100 ns.

Compound **13** showed the second most favorable binding energy value (ΔG_{bind} = −15.04 ± 4.22 kcal mol^{-1}). For this complex, the electrostatic contribution played an important role (ΔE_{ele} = −42.16 ± 4.85 kcal mol^{-1}), but its stabilizing effect was partially compensated by the unfavorable solvation contribution (ΔG_{solv} = 55.63 ± 3.61 kcal mol^{-1}).

The reference inhibitor **NNGH** showed a weakly favorable average binding energy (ΔG_{bind} = −2.98 ± 4.07 kcal·mol^{-1}). Despite the presence of stabilizing interactions, its gas-phase contribution was largely compensated by the unfavorable solvation effect.

For **19**, a positive value of ΔG_{bind} = 9.54 ± 7.66 kcal·mol^{-1} was obtained. In this complex, the favorable van der Waals contribution was insufficient to compensate for the unfavorable electrostatic and solvation components. This result may indicate a less-than-optimal stabilization of the complex in the studied conformation during the analyzed interval of the trajectory.

The overall order of the complexes by calculated MM/PBSA binding (Figure 9) energy was as follows:

17 > 13 > NNGH > 19.

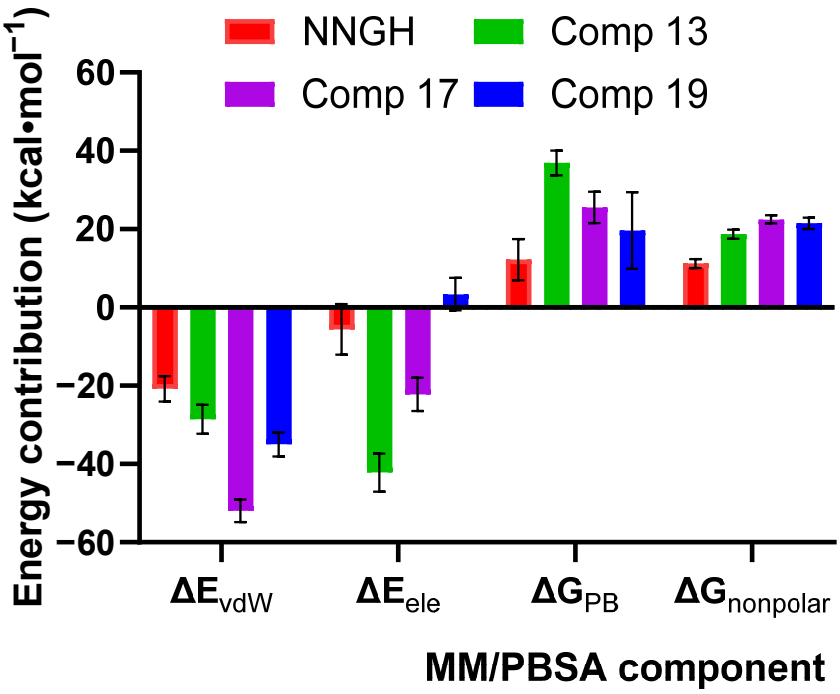

Figure 9. Energy decomposition of MM/PBSA contributions for MMP-9 complexes.

According to the results of the initial screening at a concentration of 10 μM, the studied compounds demonstrated pronounced differences in both the potency of inhibition and the profile of action against MMP-2 and MMP-9 (Table 5).

Table 5. In vitro inhibitory activity of the investigated 1,2,4-triazole derivatives against MMP-2 and MMP-9 at 10 μM.

Compound	MMP-2 * Inhibition, %	MMP-9 * Inhibition, %	Inhibition Profile **
2	12.1 ± 2.0	35.7 ± 3.5	Weak activity with MMP-9 preference
6	33.8 ± 1.7	68.7 ± 3.6	MMP-9-preferential
7	28.4 ± 3.2	72.5 ± 4.1	MMP-9-preferential
9	45.7 ± 1.1	57.8 ± 2.6	Weak activity with MMP-9 preference
13	8.3 ± 1.4	85.2 ± 3.8	Strongly MMP-9-preferential
15	56.2 ± 2.9	63.1 ± 3.3	Moderate balanced dual inhibition
17	14.8 ± 2.1	94.2 ± 4.8	Strongly MMP-9-preferential
18	32.6 ± 2.9	61.8 ± 3.2	MMP-9-preferential
19	74.2 ± 4.4	79.2 ± 2.8	Strong balanced dual inhibition
NNGH	78.1 ± 3.1	84.5 ± 2.5	Reference control

Note: * Values are presented as mean ± SD (n = 3). **NNGH** was used as the reference MMP inhibitor. ** Inhibition profiles were assigned from the relative inhibition of MMP-2 and MMP-9 observed at the screening concentration of 10 μM and should not be interpreted as definitive isoenzyme selectivity, which requires comparison of the corresponding IC_{50} values.

The highest inhibitory activity against MMP-9 was shown by **17**—94.2 ± 4.8%, which numerically exceeded the effect of the reference inhibitor **NNGH**—84.5 ± 2.5%. At the same time, the inhibition of MMP-2 for **17** was only 14.8 ± 2.1%, which indicates a pronounced predominance of action against MMP-9. A similar profile was observed for **13**, which suppressed MMP-9 by 85.2 ± 3.8% with a minimal effect on MMP-2—8.3 ± 1.4%. The difference between the inhibition of MMP-9 and MMP-2 for **17** and **13** was 79.4 and 76.9 percentage points, respectively, which allowed them to be identified as the most promising MMP-9-preferring inhibitors of the series.

A limitation of the present study is the lack of in vivo and experimental toxicity studies, which were beyond the scope of the current work. In accordance with the 3Rs principle, the present in silico and in vitro screening was used to prioritize the most promising candidates and thereby reduce the number of animals required for subsequent studies. In vivo safety and wound-healing efficacy studies of compounds **13**, **17**, and **19** are planned as the next stage of the project.

4. Conclusions

A structurally diverse series of novel orotic acid–1,2,4-triazole hybrids was successfully synthesized through selective S-functionalization of the triazole scaffold, affording the target compounds in 54–87% yields, with their structures confirmed by $^{1}H/^{13}C$ NMR spectroscopy, LC-MS, and elemental analysis. The derivatives exhibited generally acceptable drug-like properties without Lipinski-rule violations or PAINS alerts, supporting their further development, particularly for topical applications. Integrated molecular docking, interaction profiling, 100 ns molecular dynamics, and MM/PBSA analysis identified **13**, **17**, and **19** as the most promising candidates for MMP-9 modulation. Compound **17** showed the highest docking affinity for MMP-9 (-9.65 kcal·mol^{-1}) and the most favorable MM/PBSA binding-energy estimate (-26.16 ± 5.17 kcal·mol^{-1}), whereas **13** demonstrated the greatest conformational stability, with a median ligand RMSD of 0.261 nm and persistent proximity to the catalytic Zn^{2+} ion at 0.211 nm during the final 20 ns. In vitro screening at 10 μM confirmed pronounced MMP-9-preferential activity for **17** and **13**, which inhibited MMP-9 by $94.2 \pm 4.8\%$ and $85.2 \pm 3.8\%$, respectively, while producing only $14.8 \pm 2.1\%$ and $8.3 \pm 1.4\%$ inhibition of MMP-2; **19** exhibited a distinct balanced profile, inhibiting MMP-2 and MMP-9 by $74.2 \pm 4.4\%$ and $79.2 \pm 2.8\%$, respectively. Collectively, these findings establish **13** and **17** as priority MMP-9-preferential leads and **19** as a potential dual MMP-2/MMP-9 modulator.

Supplementary Materials: The following supporting information can be downloaded at https://www.mdpi.com/article/10.3390/scipharm94030065/s1. Figures S1–S21: ^{1}H and selected ^{13}C NMR spectra of compounds 1–19; Figures S22–S39: LC–MS spectra of compounds 1–19; Figures S40–S45: elemental analysis data for compounds 1–19.

Author Contributions: Conceptualization, Y.K. and V.P.; methodology, Y.K., L.K., T.C., O.B. and I.P.; software, Y.K.; validation, Y.K., V.P., L.K., T.C. and O.B.; formal analysis, Y.K., O.R. and D.S.; investigation, Y.K., L.K., T.C., O.B., I.P., D.S. and I.M.; resources, V.P., L.K., I.P. and I.B.; data curation, Y.K., O.R. and D.S.; writing—original draft preparation, Y.K.; writing—review and editing, Y.K., V.P., L.K., O.R. and I.B.; visualization, Y.K. and D.S.; supervision, V.P. and L.K.; project administration, Y.K.; funding acquisition, Y.K. All authors have read and agreed to the published version of the manuscript.

Funding: This research was supported by the National Research Foundation of Ukraine within project No. 2025.05/0022, "Hybrid compounds of 1,2,4-triazole and orotic acid with radioprotective, wound-healing, and regenerative properties for the needs of civilians and the Armed Forces of Ukraine." The study was also conducted within the framework of the research project of the Ministry of Health of Ukraine, state registration No. 0126U001480, "Development of 1,2,4-triazole derivatives with polypharmacological activity for the needs of military medicine and persons affected by hostilities".

Institutional Review Board Statement: Not applicable.

Informed Consent Statement: Not applicable.

Data Availability Statement: All data produced in this study are contained in the manuscript text and Supporting Information File.

Conflicts of Interest: The authors declare no conflicts of interest.

References

1. Cabral-Pacheco, G.A.; Garza-Veloz, I.; Castruita-De la Rosa, C.; Ramirez-Acuña, J.M.; Perez-Romero, B.A.; Guerrero-Rodriguez, J.F.; Martinez-Avila, N.; Martinez-Fierro, M.L. The Roles of Matrix Metalloproteinases and Their Inhibitors in Human Diseases. *Int. J. Mol. Sci.* **2020**, *21*, 9739. [CrossRef] [PubMed]
2. Nikolov, A.; Popovski, N. Role of Gelatinases MMP-2 and MMP-9 in Healthy and Complicated Pregnancy and Their Future Potential as Preeclampsia Biomarkers. *Diagnostics* **2021**, *11*, 480. [CrossRef] [PubMed]
3. Wolosowicz, M.; Prokopiuk, S.; Kaminski, T.W. Matrix Metalloproteinase-9 (MMP-9) as a Therapeutic Target: Insights into Molecular Pathways and Clinical Applications. *Pharmaceutics* **2025**, *17*, 1425. [CrossRef] [PubMed]
4. Van den Steen, P.E.; Dubois, B.; Nelissen, I.; Rudd, P.M.; Dwek, R.A.; Opdenakker, G. Biochemistry and Molecular Biology of Gelatinase B or Matrix Metalloproteinase-9 (MMP-9). *Crit. Rev. Biochem. Mol. Biol.* **2002**, *37*, 375–536. [CrossRef] [PubMed]
5. Vandooren, J.; Van den Steen, P.E.; Opdenakker, G. Biochemistry and molecular biology of gelatinase B or matrix metalloproteinase-9 (MMP-9): The next decade. *Crit. Rev. Biochem. Mol. Biol.* **2013**, *48*, 222–272. [CrossRef] [PubMed]
6. Vandooren, J.; Swinnen, W.; Ugarte-Berzal, E.; Boon, L.; Dorst, D.; Martens, E.; Opdenakker, G. Endotoxemia shifts neutrophils with TIMP-free gelatinase B/MMP-9 from bone marrow to the periphery and induces systematic upregulation of TIMP-1. *Haematologica* **2017**, *102*, 1671–1682. [CrossRef] [PubMed]
7. Vafadari, B.; Salamian, A.; Kaczmarek, L. MMP-9 in translation: From molecule to brain physiology, pathology, and therapy. *J. Neurochem.* **2016**, *139*, 91–114. [CrossRef] [PubMed]
8. Reinhard, S.M.; Razak, K.; Ethell, I.M. A delicate balance: Role of MMP-9 in brain development and pathophysiology of neurodevelopmental disorders. *Front. Cell. Neurosci.* **2015**, *9*, 280. [CrossRef] [PubMed]
9. Wei, T.; Zhang, H.; Cetin, N.; Miller, E.; Moak, T.; Suen, J.Y.; Richter, G.T. Elevated Expression of Matrix Metalloproteinase-9 not Matrix Metalloproteinase-2 Contributes to Progression of Extracranial Arteriovenous Malformation. *Sci. Rep.* **2016**, *6*, 24378. [CrossRef] [PubMed]
10. Bian, Y.; Xiang, Z.; Wang, Y.; Ren, Q.; Chen, G.; Xiang, B.; Wang, J.; Zhang, C.; Pei, S.; Guo, S.; et al. Immunomodulatory roles of metalloproteinases in rheumatoid arthritis. *Front. Pharmacol.* **2023**, *14*, 1285455. [CrossRef] [PubMed]
11. Kalali, D. The Role of the Matrix Metalloproteinase-9 Gene in Tumor Development and Metastasis: A Narrative Review. *Glob. Med. Genet.* **2023**, *10*, 48–53. [CrossRef] [PubMed]
12. Turner, R.J.; Sharp, F.R. Implications of MMP9 for Blood Brain Barrier Disruption and Hemorrhagic Transformation Following Ischemic Stroke. *Front. Cell. Neurosci.* **2016**, *10*, 56. [CrossRef] [PubMed]
13. Shoari, A.; Ashja Ardalan, A.; Dimesa, A.M.; Coban, M.A. Targeting Invasion: The Role of MMP-2 and MMP-9 Inhibition in Colorectal Cancer Therapy. *Biomolecules* **2025**, *15*, 35. [CrossRef] [PubMed]
14. Caley, M.P.; Martins, V.L.; O'Toole, E.A. Metalloproteinases and Wound Healing. *Adv. Wound Care* **2015**, *4*, 225–234. [CrossRef] [PubMed]
15. Matiichuk, Y.; Drapak, I.; Darmograi, N.; Bartoshyk, N.; Drapak, Y.; Matiychuk, V. Synthesis and biological activity of rhodanine-furan conjugates: A review. *Curr. Chem. Lett.* **2024**, *13*, 287–302. [CrossRef]
16. Laronha, H.; Carpinteiro, I.; Portugal, J.; Azul, A.; Polido, M.; Petrova, K.T.; Salema-Oom, M.; Caldeira, J. Challenges in Matrix Metalloproteinases Inhibition. *Biomolecules* **2020**, *10*, 717. [CrossRef] [PubMed]
17. Vandenbroucke, R.; Libert, C. Is there new hope for therapeutic matrix metalloproteinase inhibition? *Nat. Rev. Drug Discov.* **2014**, *13*, 904–927. [CrossRef] [PubMed]
18. Fabre, B.; Ramos, A.; de Pascual-Teresa, B. Targeting Matrix Metalloproteinases: Exploring the Dynamics of the S1′ Pocket in the Design of Selective, Small Molecule Inhibitors. *J. Med. Chem.* **2014**, *57*, 10205–10219. [CrossRef] [PubMed]
19. Rashid, Z.A.; Bardaweel, S.K. Novel Matrix Metalloproteinase-9 (MMP-9) Inhibitors in Cancer Treatment. *Int. J. Mol. Sci.* **2023**, *24*, 12133. [CrossRef] [PubMed]
20. Lein, M.; Jung, K.; Ortel, B.; Stephan, C.; Rothaug, W.; Juchem, R.; Johannsen, M.; Deger, S.; Schnorr, D.; Loening, S.; et al. The new synthetic matrix metalloproteinase inhibitor (Roche 28-2653) reduces tumor growth and prolongs survival in a prostate cancer standard rat model. *Oncogene* **2002**, *21*, 2089–2096. [CrossRef] [PubMed]
21. Severin, O.; Pilyo, S.; Semenyuta, I.; Kachaeva, M.; Zhirnov, V.; Brovaret, V. Design, synthesis and anticancer activity of novel 4-(5-amino-4-cyano-1,3-oxazol-2-yl)benzenesulfonamide derivatives. *Curr. Chem. Lett.* **2025**, *14*, 159–172. [CrossRef]
22. Albelwi, F.F.; Teleb, M.; Abu-Serie, M.M.; Moaty, M.N.A.A.; Alsubaie, M.S.; Zakaria, M.A.; El Kilany, Y.; Aouad, M.R.; Hagar, M.; Rezki, N. Halting Tumor Progression via Novel Non-Hydroxamate Triazole-Based Mannich Bases MMP-2/9 Inhibitors; Design, Microwave-Assisted Synthesis, and Biological Evaluation. *Int. J. Mol. Sci.* **2021**, *22*, 10324. [CrossRef] [PubMed]
23. Yurttaş, L.; Evren, A.S.A.F.; Kubilay, A.; Temel, H. Synthesis of New 1,2,4-Triazole Derivatives and Evaluation of Their MMP-9 Inhibition Activity. *Acta Pharm. Sci.* **2021**, *59*, 215–232. [CrossRef]

24. Hariono, M.; Nuwarda, R.F.; Yusuf, M.; Rollando, R.; Jenie, R.I.; Al-Najjar, B.; Julianus, J.; Putra, K.C.; Nugroho, E.S.; Wisnumurti, Y.K.; et al. Arylamide as Potential Selective Inhibitor for Matrix Metalloproteinase 9 (MMP9): Design, Synthesis, Biological Evaluation, and Molecular Modeling. *J. Chem. Inf. Model.* **2020**, *60*, 349–359. [CrossRef] [PubMed]
25. Dufour, A.; Sampson, N.S.; Li, J.; Kuscu, C.; Rizzo, R.C.; Deleon, J.L.; Zhi, J.; Jaber, N.; Liu, E.; Zucker, S.; et al. Small-molecule anticancer compounds selectively target the hemopexin domain of matrix metalloproteinase-9. *Cancer Res.* **2011**, *71*, 4977–4988, Correction in *Cancer Res.* **2012**, *72*, 5141–5142. [CrossRef] [PubMed]
26. Alford, V.M.; Kamath, A.; Ren, X.; Kumar, K.; Gan, Q.; Awwa, M.; Tong, M.; Seeliger, M.A.; Cao, J.; Ojima, I.; et al. Targeting the Hemopexin-like Domain of Latent Matrix Metalloproteinase-9 (proMMP-9) with a Small Molecule Inhibitor Prevents the Formation of Focal Adhesion Junctions. *ACS Chem. Biol.* **2017**, *12*, 2788–2803. [CrossRef] [PubMed]
27. Yurttaş, L.; Evren, A.E.; Kubilay, A.; Temel, H.E.; Çiftçi, G.A. 3,4,5-Trisubstituted-1,2,4-Triazole Derivatives as Antiproliferative Agents: Synthesis, In Vitro Evaluation and Molecular Modelling. *Lett. Drug Des. Discov.* **2020**, *17*, 1502–1515. [CrossRef]
28. Karpenko, Y.; Medvedeva, K.; Solomennyi, A.; Rudenko, O.; Panasenko, O.; Parchenko, V.; Vasyuk, S. Design, synthesis, molecular docking, and antioxidant properties of a series of new S-derivatives of ((1,2,4-triazol-3(2H)-yl)methyl)thiopyrimidines. *Sci. Pharm. Sci.* **2025**, *1*, 62–70. [CrossRef]
29. Karpenko, Y.; Parchenko, V.; Panasenko, O.; Bihdan, O.; Pukhalska, I.; Nikiforov, O.; Nahorna, N.; Nahornyi, V.; Roik, O. Novel 1,2,4-Triazole–Thiopyrimidine Hybrids as COX-2 Inhibitors: Synthesis, ADME Profiling, Antioxidant Activity, and Molecular Docking. *BioMed Res. Int.* **2026**, *2026*, 4477854. [CrossRef] [PubMed]
30. Kucherenko, L.I.; Karpenko, Y.V.; Ohloblina, M.V.; Zazharskyi, V.V.; Bilan, M.V.; Kulishenko, O.M.; Bushuieva, I.V.; Parchenko, V.V. Monitoring the properties of 1,2,4-triazole derivatives for the development of original antimicrobial drugs. *Zaporozhye Med. J.* **2024**, *26*, 481–489. [CrossRef]
31. Myrko, I.; Chaban, T.; Demchuk, Y.; Drapak, Y.; Chaban, I.; Drapak, I.; Pankiv, M.; Matiychuk, V. Current trends of chemoinformatics and computer chemistry in drug design: A review. *Curr. Chem. Lett.* **2024**, *13*, 151–162. [CrossRef]
32. Daina, A.; Michielin, O.; Zoete, V. SwissADME: A Free Web Tool to Evaluate Pharmacokinetics, Drug-Likeness and Medicinal Chemistry Friendliness of Small Molecules. *Sci. Rep.* **2017**, *7*, 42717. [CrossRef] [PubMed]
33. Burley, S.K.; Piehl, D.W.; Vallat, B.; Zardecki, C. RCSB Protein Data Bank: Supporting Research and Education Worldwide through Explorations of Experimentally Determined and Computationally Predicted Atomic-Level 3D Biostructures. *IUCrJ* **2024**, *11*, 279–286. [CrossRef] [PubMed]
34. Karpun, Y.; Fedotov, S.; Khilkovets, A.; Karpenko, Y.; Parchenko, V.; Klochkova, Y.; Bila, Y.; Lukina, I.; Nahorna, N.; Nahornyi, V. An in silico investigation of 1,2,4-triazole derivatives as potential antioxidant agents using molecular docking, MD simulations, MM-PBSA free energy calculations and ADME predictions. *Pharmacia* **2023**, *70*, 139–153. [CrossRef]
35. O'Boyle, N.M.; Banck, M.; James, C.A.; Morley, C.; Vandermeersch, T.; Hutchison, G.R. Open Babel: An Open Chemical Toolbox. *J. Cheminform.* **2011**, *3*, 33. [CrossRef] [PubMed]
36. Koes, D.R.; Baumgartner, M.P.; Camacho, C.J. Lessons Learned in Empirical Scoring with smina from the CSAR 2011 Benchmarking Exercise. *J. Chem. Inf. Model.* **2013**, *53*, 1893–1904. [CrossRef] [PubMed]
37. Eberhardt, J.; Santos-Martins, D.; Tillack, A.F.; Forli, S. AutoDock Vina 1.2.0: New Docking Methods, Expanded Force Field, and Python Bindings. *J. Chem. Inf. Model.* **2021**, *61*, 3891–3898. [CrossRef] [PubMed]
38. Adasme, M.F.; Linnemann, K.L.; Bolz, S.N.; Kaiser, F.; Salentin, S.; Haupt, V.J.; Schroeder, M. PLIP 2021: Expanding the Scope of the Protein–Ligand Interaction Profiler to DNA and RNA. *Nucleic Acids Res.* **2021**, *49*, W530–W534. [CrossRef] [PubMed]
39. Schrödinger LLC. *The PyMOL Molecular Graphics System*; Schrödinger, LLC: New York, NY, USA, 2015.
40. Schrödinger LLC. *Maestro*; Schrödinger, LLC: New York, NY, USA, 2020.
41. Karpenko, Y.V.; Panasenko, O.I.; Zazharsky, V.V.; Parchenko, V.V.; Pidlisny, O.V.; Yaroshenko, I.V.; Bilan, M.V.; Davydenko, P.O.; Kulishenko, O.M.; Zazharska, N.M. Synthesis, Chemical Properties and Search for Molecular Descriptors of the Fungicidal Activity of New Hybrids of 1,2,4-Triazole(1,3,4-Oxadiazole) Bearing a Pyrimidine Fragment. *Vopr. Khim. Khim. Tekhnol.* **2025**, *161*, 58–69. [CrossRef]
42. Jo, S.; Kim, T.; Iyer, V.G.; Im, W. CHARMM-GUI 10 Years for Biomolecular Modeling and Simulation. *J. Comput. Chem.* **2017**, *38*, 1114–1124. [CrossRef] [PubMed]
43. Huang, J.; Rauscher, S.; Nawrocki, G.; Ran, T.; Feig, M.; de Groot, B.L.; Grubmüller, H.; MacKerell, A.D. CHARMM36m: An Improved Force Field for Folded and Intrinsically Disordered Proteins. *Nat. Methods* **2017**, *14*, 71–73. [CrossRef] [PubMed]
44. Vanommeslaeghe, K.; Hatcher, E.; Acharya, C.; Kundu, S.; Zhong, S.; Shim, J.; Darian, E.; Guvench, O.; Lopes, P.; Vorobyov, I.; et al. CHARMM General Force Field: A Force Field for Drug-Like Molecules Compatible with the CHARMM All-Atom Additive Biological Force Fields. *J. Comput. Chem.* **2010**, *31*, 671–690. [CrossRef] [PubMed]
45. Páll, S.; Zhmurov, A.; Bauer, P.; Abraham, M.; Lundborg, M.; Gray, A.; Hess, B.; Lindahl, E. Heterogeneous Parallelization and Acceleration of Molecular Dynamics Simulations in GROMACS. *J. Chem. Phys.* **2020**, *153*, 134110. [CrossRef] [PubMed]

46. Valdés-Tresanco, M.S.; Valdés-Tresanco, M.E.; Valiente, P.A.; Moreno, E. gmx_MMPBSA: A New Tool to Perform End-State Free Energy Calculations with GROMACS. *J. Chem. Theory Comput.* **2021**, *17*, 6281–6291. [CrossRef] [PubMed]
47. Yuriy, K.; Tüzün, G.; Volodymyr, P.; Köse, F.A.; Myroslava, O.; Yıldırım, Ş.; Inna, B.; Kocyigit, U.M.; Anastasia, K.; Tüzün, B.; et al. Cytotoxic potential of novel triazole-based hybrids: Design, synthesis, in silico evaluation, and in vitro assessment against cancer cell lines. *Bioorganic Chem.* **2025**, *163*, 108749. [CrossRef] [PubMed]